- Supplementary Information -

Insights into zero-gap CO_2 electrolysis at elevated temperatures

Carlos A. Giron Rodriguez,[a] Nishithan Kani,[a] Asger B. Moss,[a] Bjørt Oladottir Joensen,[a] Sahil Garg,[a] Wanyu Deng,[a] Terry Wilson[b], John R. Varcoe[b], Ib Chorkendorff,[a] and Brian Seger[a]*

[a]*Surface Physics and Catalysis (SURFCAT) Section, Department of Physics, Technical University of Denmark, 2800 Kgs. Lyngby, Denmark*

[b]*Department of Chemistry, University of Surrey, Guildford GU2 7XH, United Kingdom*

**Correspondence to: Brian Seger, Email: brse@fysik.dtu.dk*

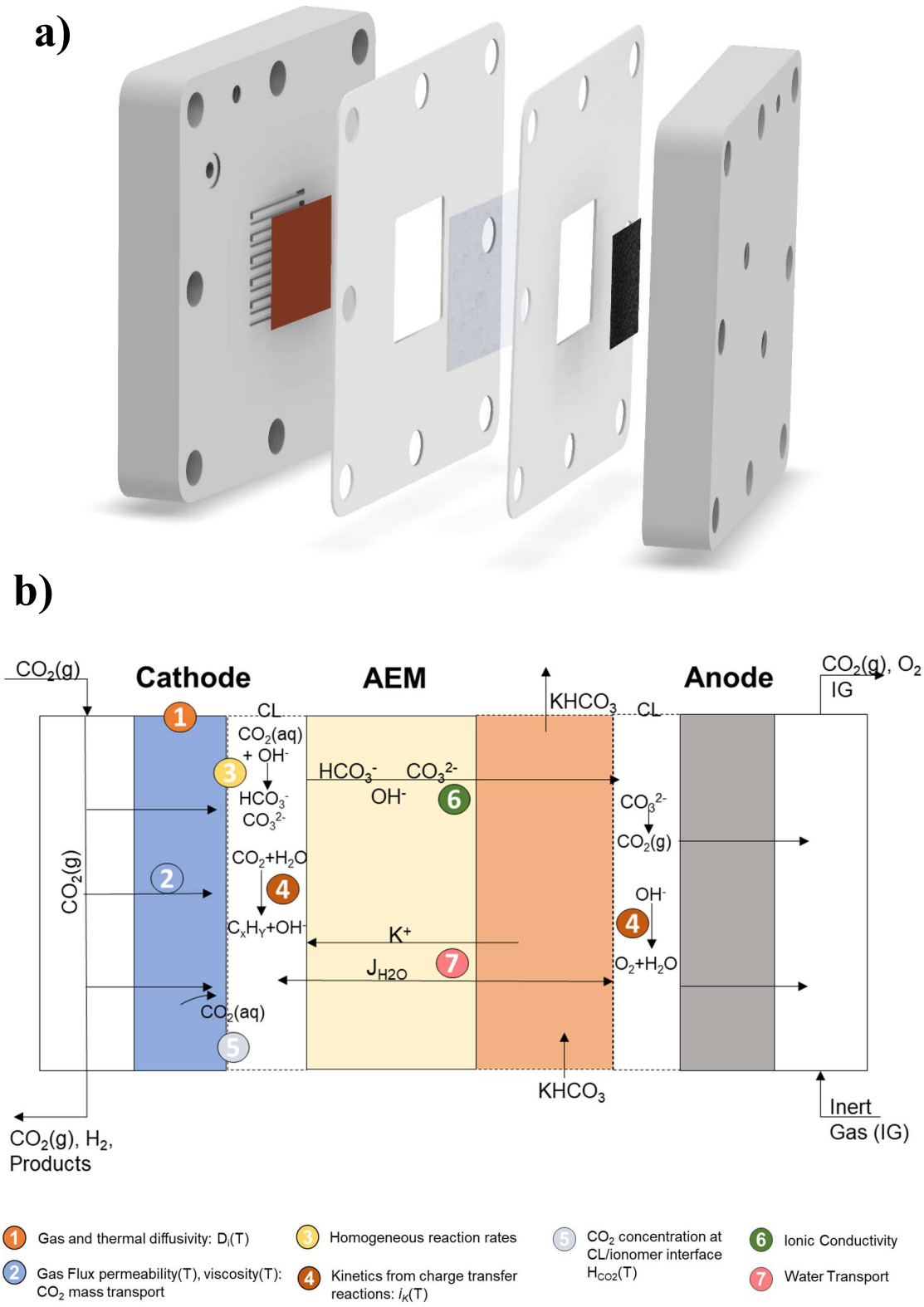

Figure S1. a) MEA cell drawing of CO_2 electrolyzer b). Schematic representation of the CO_2R in MEA configuration and main properties/parameters influenced by the temperature.

Influence of transport properties in CO_2 electrolysis as effect of temperature:

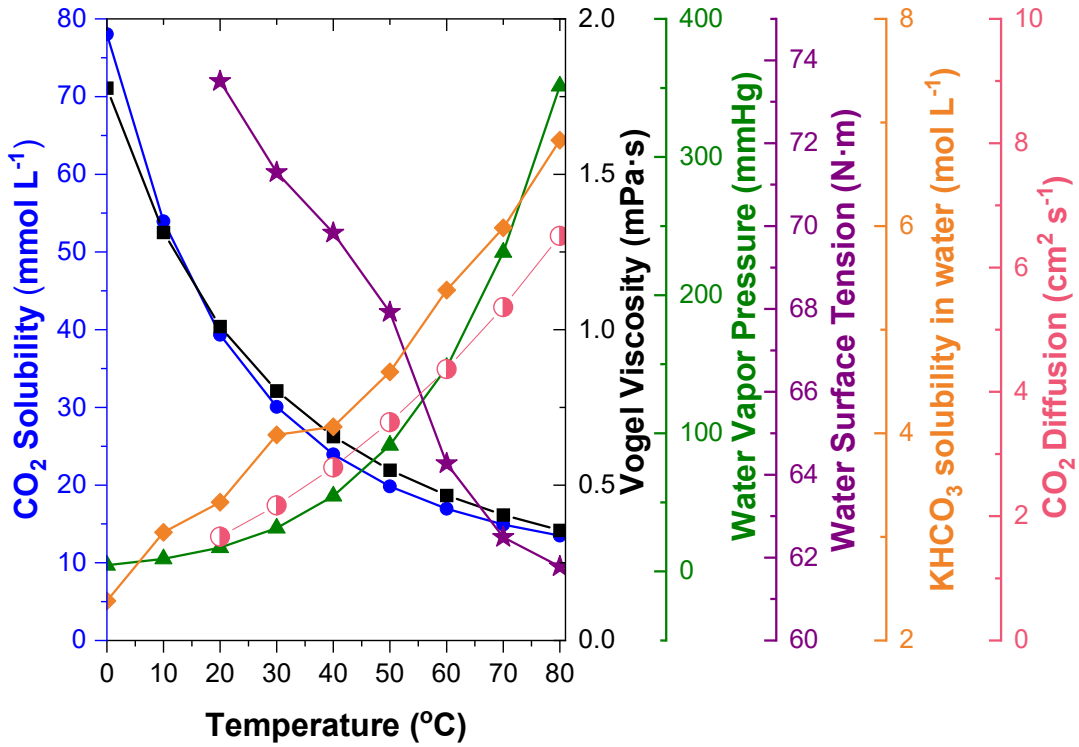

Figure S2. Transport and kinetics factor's temperature dependency on CO_2R (CO_2 solubility, CO_2 diffusion, water vapor pressure, surface tension, vogel viscosity, salt solubility, and Henry's constant).

CO_2 Solubility (in aqueous environment)[1]:

$$c_{CO2} = H_{CO2} * c_{CO2,gas} \quad \textbf{(Eq S. 1)}$$

$$H_{CO2}\,(mM/atm) = 93{,}4517 \cdot \left(\frac{100}{\mathrm{T[K]}}\right) - 60{,}2409 + \left(23{,}3585 \cdot \log\left(\frac{T[K]}{100}\right)\right) \quad \textbf{(Eq S. 2)}$$

CO_2 Diffusion[2]:

$$D_{CO2}(cm^2/\mathrm{s}) = 2{,}17 \cdot 10^{-4} \cdot \mathrm{e}^{\left(-\frac{2345}{\frac{1}{\mathrm{T[K]}}+\frac{1}{\mathrm{T_{ref}}}}\right)} \quad \textbf{(Eq S. 3)}$$

Vogel Viscosity[3]:

$$\vartheta\,(mPa \cdot \mathrm{s}) = e^{-3{,}6413+542{,}\frac{05}{T[K]-144{,}15}} \quad \textbf{(Eq S. 4)}$$

Water vapor pressure[2,4]:

$$p_{H2O}(mmHg) = 10^{8{,}07\ \left(\frac{1730{,}63}{T[K]-39{,}724}\right)} \quad \textbf{(Eq S. 5)}$$

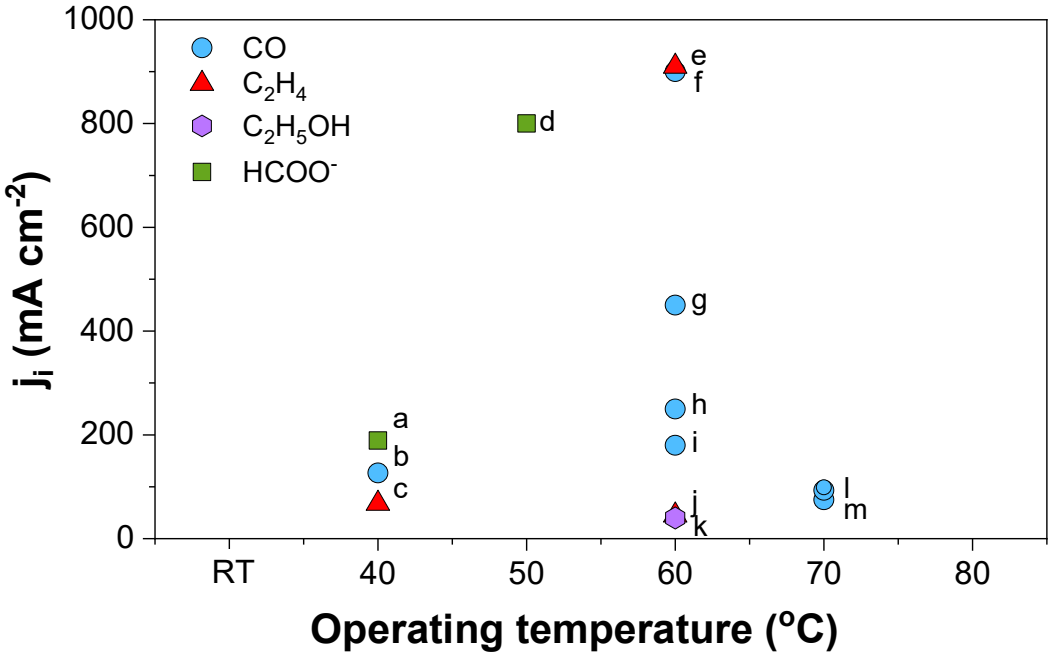

Figure S3. Summary of studies for CO_2E performed at elevated temperatures reported in the literature. (See Table S1 for the detailed information of the data). j_i corresponds to the partial current density of derived CO_2-product (CO, formate, ethanol and ethylene).

Table S1. Compiled data of different studies for CO_2 electrolysis performed at elevated temperatures and industrial relevant conditions

	Author	Year	Cathode	Anode	IEM	Type	Electrolyte	j_{total} (mA cm^{-2})	E_{cell} (V)	T (°C)	Cell Conf.	FE (%)
a	Endrodi et al.[5]	2020	Ag NPs on CP	IrOx-Ti	AEM	PiperION	0,1 CsOH	1000	2.6-3.4	60	MEA	90% CO
b	Dufek et al.[6]	2012	Ag GDE	RuOx	AEM	Excellion	2.5 M KOH	125	3.3	70	Flow Cell	60% CO
c	Yin et al.[7]	2019	Au	Ti-Sheet	AEM	QAPPT Membrane	Pure Water	500	3	60	MEA	90% CO
d	Yin et al.[7]	2019	CoPc	Ti-Sheet	AEM	QAPPT Membrane	Pure Water	200	2.8	60	MEA	90% CO
e	Pribyl-Kranewitter[8]	2021	Ag-GDE 29BC	$IrTiO_2$-Nafion	BPM	Fumasep BPM	DI Water	136	2.9	40	Flow Cell	93% CO
f	Gabardo et al.[9]	2019	Cu-GDE	IrO_2	AEM	Sustainion X37-50	0.1 M $KHCO_3$	150	4	40	MEA	45% C_2H_4
g	Gabardo et al.[9]	2019	Cu-GDE	IrO_2	AEM	Sustainion X37-50	0.1 M $KHCO_3$	100	3.7	60	MEA	30% C_2H_4
h	Kai Miao et al.[10]	2021	Cu-GDE in PTFE	IrO_2/Ti	AEM	Sustainion, PiperION	0.1 M $KHCO_3$	200	3.85	60	MEA	20% EtOH
i	Lee et al.[11]	2018	Sn-NPs on CP	Pt Black	CEM	Nafion 115	1 M $KHCO_3$ /1 M KOH	100	2.2	70	Flow Cell	93.3% $HCOO^-$
j	Li et al.[12]	2007	Sn NPs	Ti Mesh	CEM	Nafion 117	0,5 M $KHCO_3$+ 2 M KCl	310	3.9	40	Flow Cell	61% $HCOO^-$
k	Dufek et al.[13]	2014	Ag GDE	Ir-Ni mesh	CEM	Nafion 115	0,5 M K_2SO_4	275	3.4-3.6	60	Flow Cell	90% CO
l	Dufek et al.[6]	2011	Ag-GDE	Ru- DSA	CEM	Nafion 424	0,8 M K_2SO_4	110	1.57	70	Flow Cell	90% CO
m	Jeng and Jiao[14]	2020	Ag-GDE	IrO_2	AEM	Sustainion	0.05 M $KHCO_3$	200	3.1	60	MEA	90% CO
n	Garcia de Arquer et al.[1]	2020	Cu-CIBH	Ni Foam	AEM	Fumasep FA-PK 130	7 M KOH	1400	5.5	60	Flow Cell	65% C_2H_4
o	Lowe et al.[15]	2019	Sn-GDE	Ni Gauze	CEM	Nafion 117	2 M $KHCO_3$	1000	1.72 V SHE	50	Flow Cell	80% HCOO-

Scheme of configurations to evaluate the effect of the heating method

a). Use of heating rods connected to the flow field on both compartments

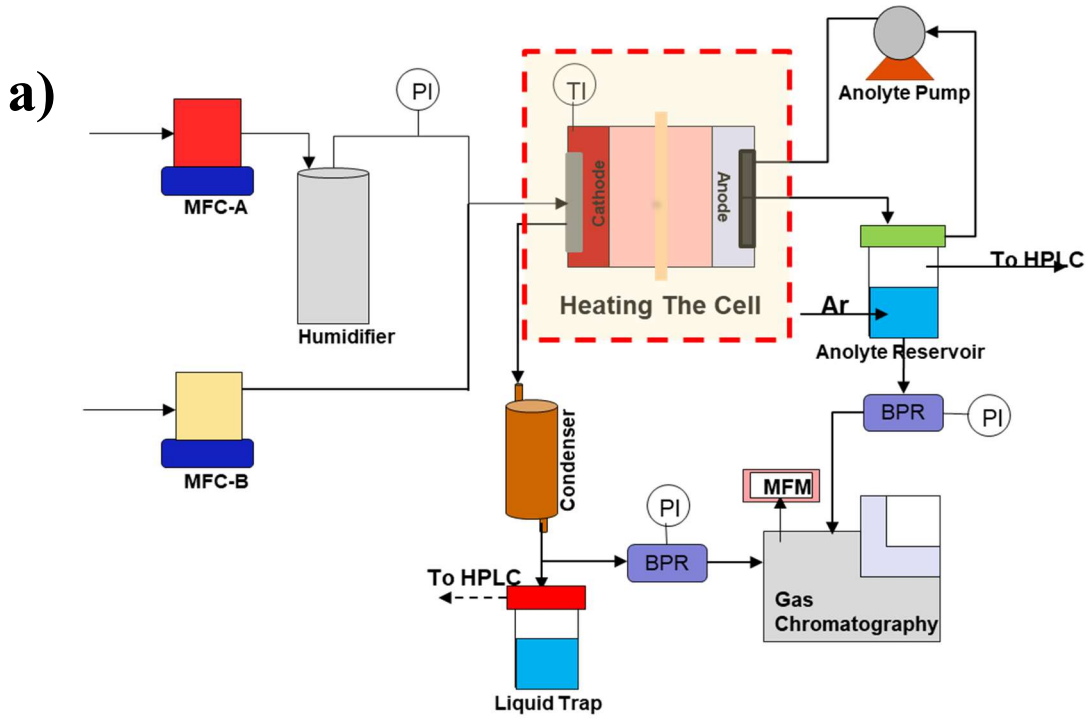

b). Use of a heating plate for the electrolyte reservoir heating

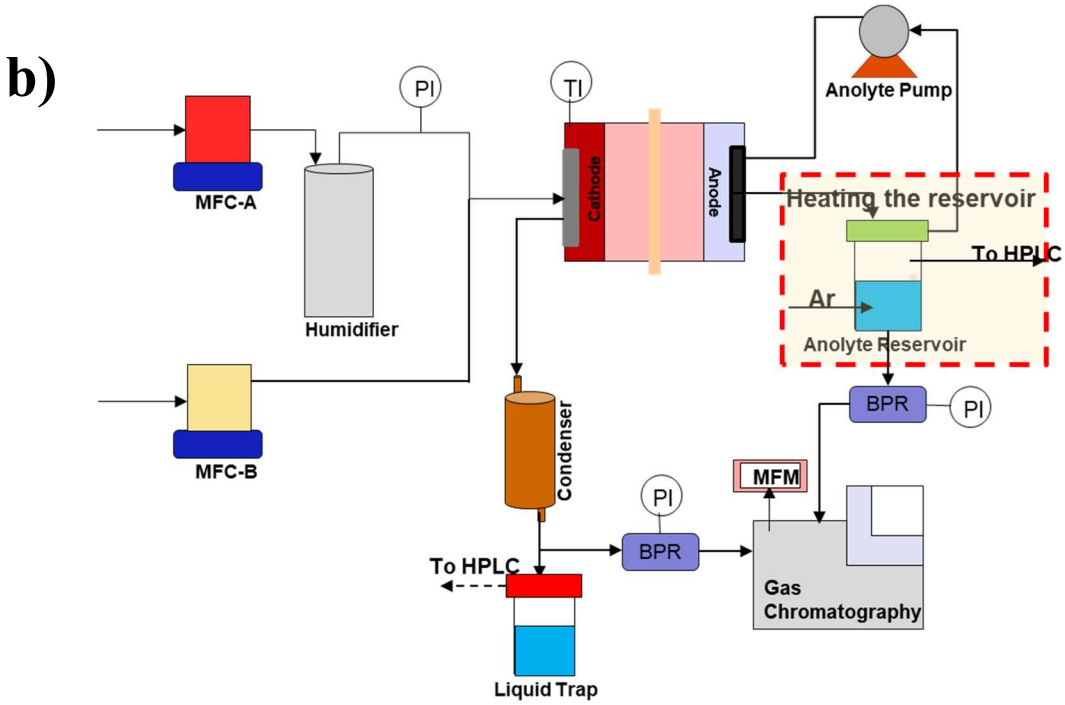

Figure S4. Schematic representation of heating methods a), Heating the EC and b) Anolyte

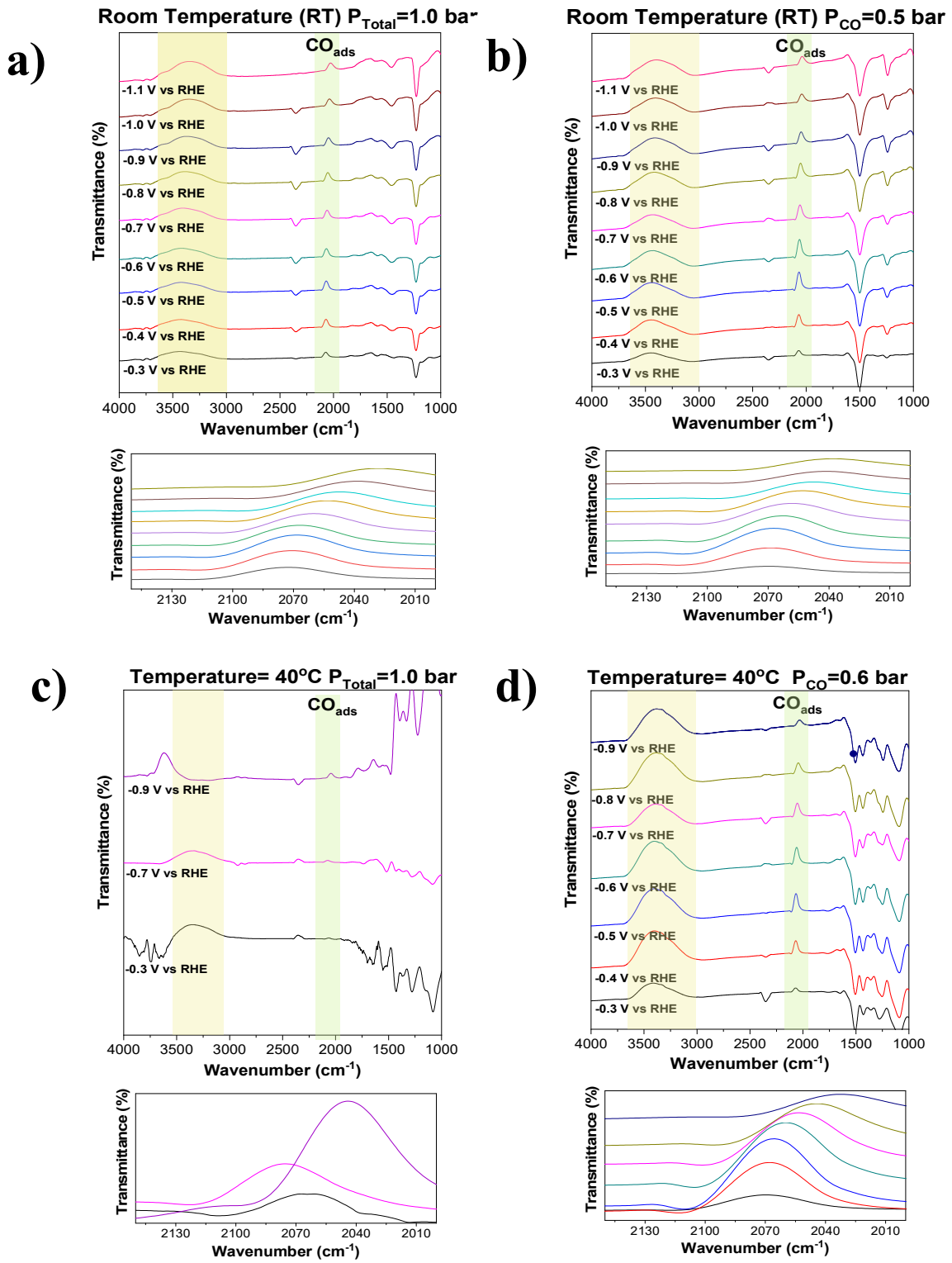

Figure S5. Full ATR-SEIRAS for CO electrolysis at different cathodic potentials at different temperatures and partial pressures a). room temperature b). room temperature and P_{CO}=0.5 bar c). 40 °C and d). 40 °C and P_{CO}=0.6 bar

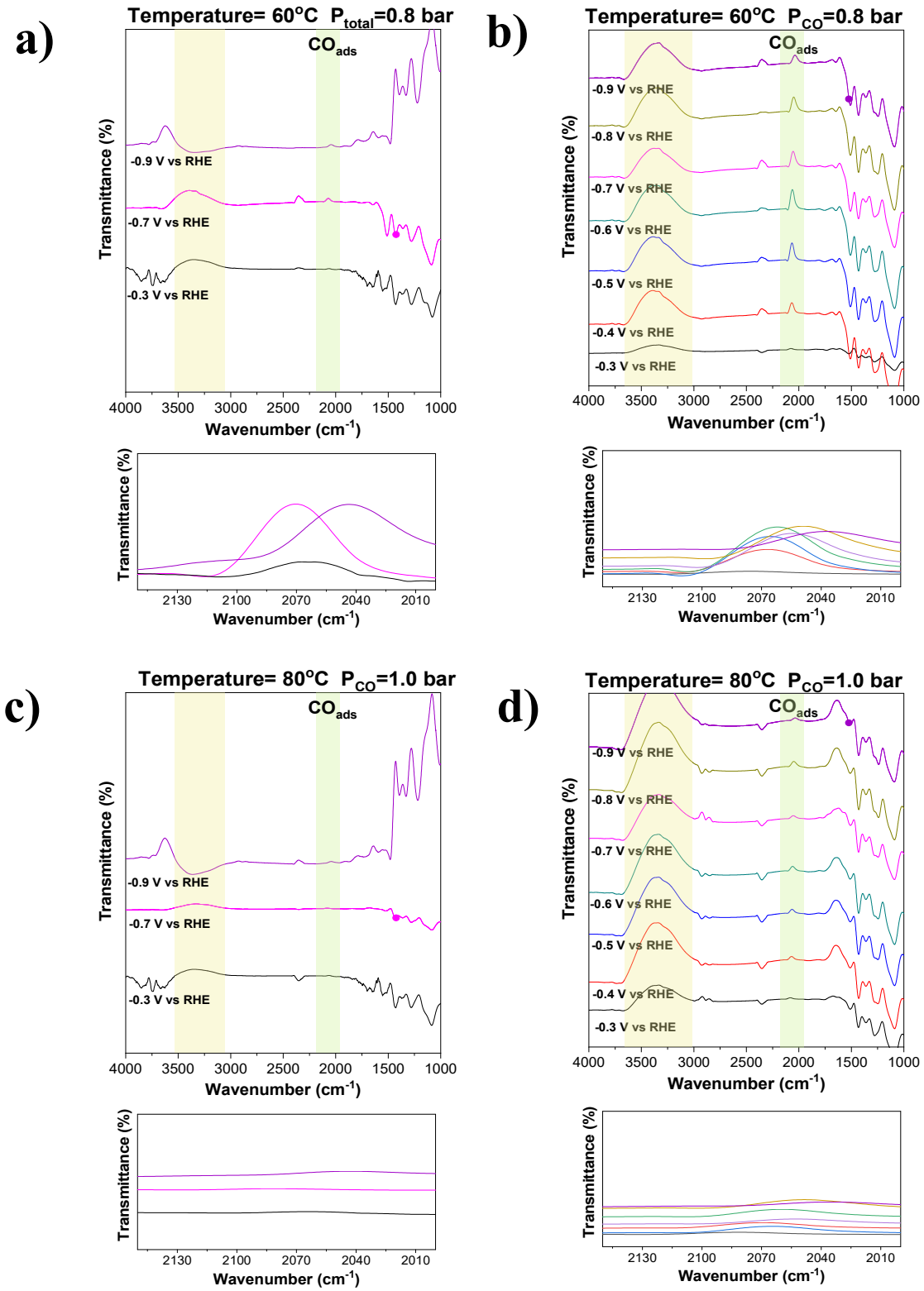

Figure S6. Full ATR-SEIRAS for CO electrolysis at different cathodic potentials at different temperatures and partial pressures a). 60 °C b). 60 °C and P_{CO}=0.8 bar c). 80 °C, and d). 80 °C and P_{CO}=1.0 bar

Effect of temperature on CO solubility

Empirical expression for CO concentration in aqueous solutions as the effect of the temperature.[21]

$$c_{CO}\left(\frac{mol}{kg\ bar}\right) = 9.9\ \cdot 10^{-4}\ \cdot \exp\left(1300 \cdot \frac{1}{T[K]} - \frac{1}{298}\right) \quad \textbf{(Eq S. 12)}$$

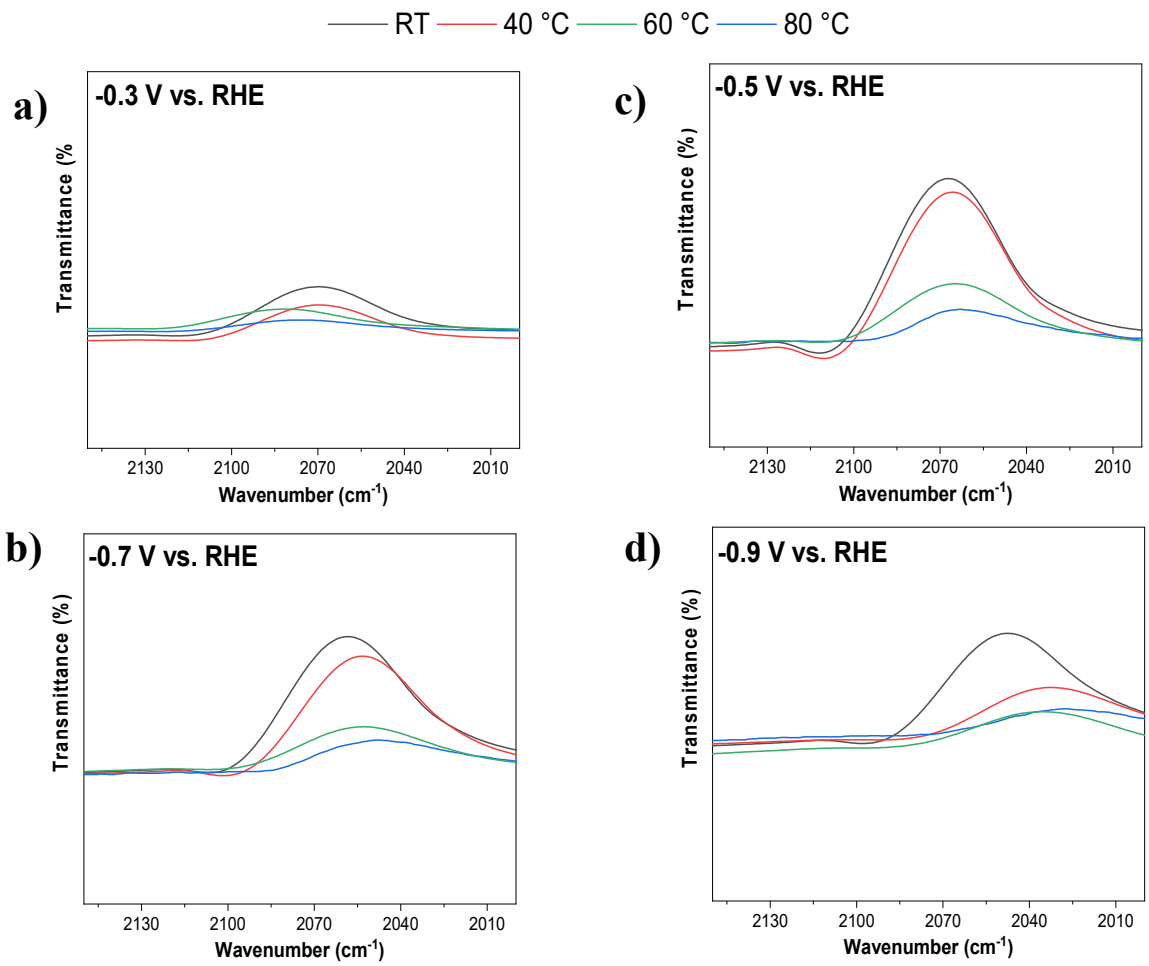

Figure S7. CO features from ATR-SEIRAS spectra at different temperatures as a function of the cathodic potentials a). -0.3 V b). -0.5 V c) -0.7 V and d). -0.9 V vs. RHE. Value of partial pressure are (0.5 bar for RT, 0.6 bar for 40°C, 0.8 bar for 70°C and 1 bar for 80°C).

Supplementary Note I

Estimation of the standard equilibrium potentials

$$\Delta G^0 = -z\,F\,E^0_{cell} \quad (\mathbf{Eq\ S.6})$$

In Equation (Eq S.6), z corresponds to the moles of electrons, F the Faraday's constant, ΔG^0 the Gibbs free energy related to the electrical work and E^0_{cell} is the standard cell potential. The thermochemistry data for carbon products from CO_2R can be found from literature[16]

Table S2. Thermodynamic data of standard enthalpy and entropy for different CO_2-derived products

Product (Phase)	**E (V vs. RHE)**	**z**	$\Delta H^0\ (kJ\ mol^{-1})$	S^0 $(J\ mol^{-1}\ K^{-1})$
CO (g)	-0.10	2	-110.5	197.66
HCOOH (aq)	-0.12	2	-425.5	129
CH_4 (g)	0.17	8	-74.6	186.3
CH_3COOH (aq)	0.11	8	-483.5	158
C_2H_5OH (l)	0.09	12	-277.7	281.6
C_2H_4 (g)	0.08	12	52.5	219.32
C_3H_7OH (l)	0.0	18	-255.22	192.8
H_2 (g)	0	2	0	130.7
H_2O (l)	-	-	-285.5	69.9
CO_2 (g)	-	-	-393.5	213.57

Table S3. Effect of operating temperature in the standard potentials for different CO_2R products

Temperature (°C)	E° CO (V)	E° C_2H_4 (V)	E° EtOH (V)	E° PrOH (V)	E° CH_4 (V)
20	-0.104	0.081	0.080	0.096	0.171
30	-0.108	0.075	0.074	0.090	0.165
40	-0.112	0.069	0.068	0.083	0.160
50	-0.116	0.062	0.062	0.077	0.155
60	-0.120	0.056	0.056	0.070	0.150
70	-0.123	0.050	0.049	0.063	0.144
80	-0.127	0.044	0.043	0.057	0.139

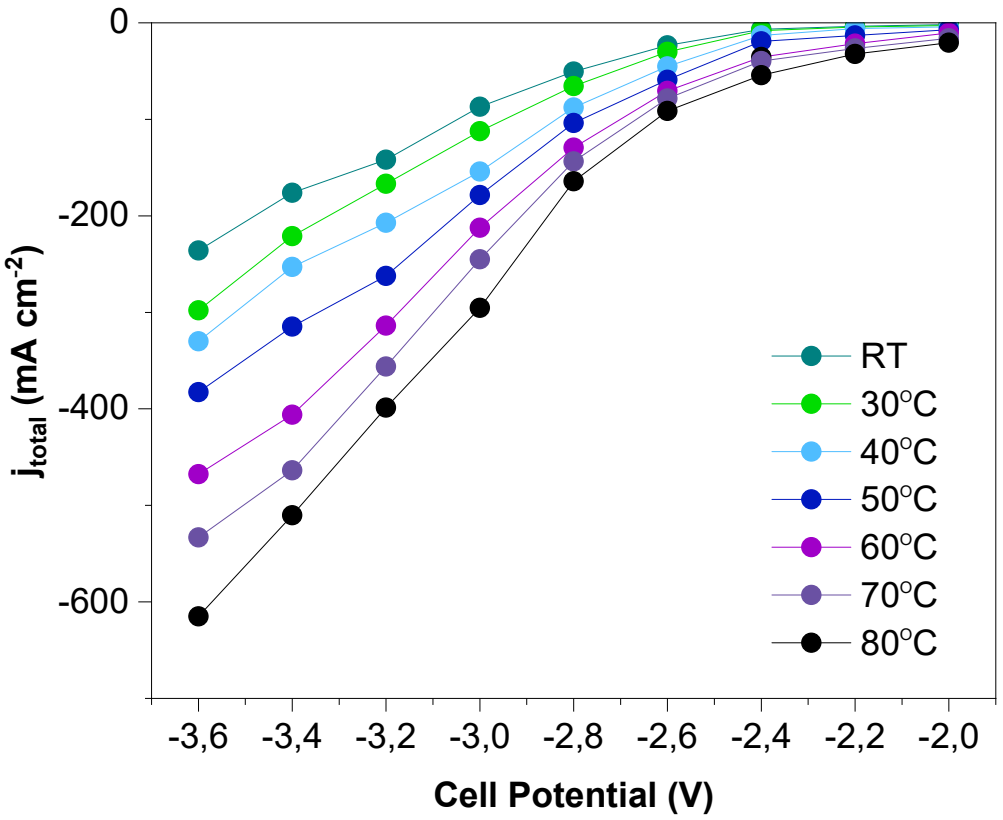

Figure S8. Chronoamperiometry measurements of CO_2 electrolysis at different cell potentials and temperatures in prior experiments. (Experimental conditions: Cu-GDE (Cathode), MPIP-AEM, IO_2 (Anode), O_2 feeding rate 40 sccm, 0.1 M $KHCO_3$) .

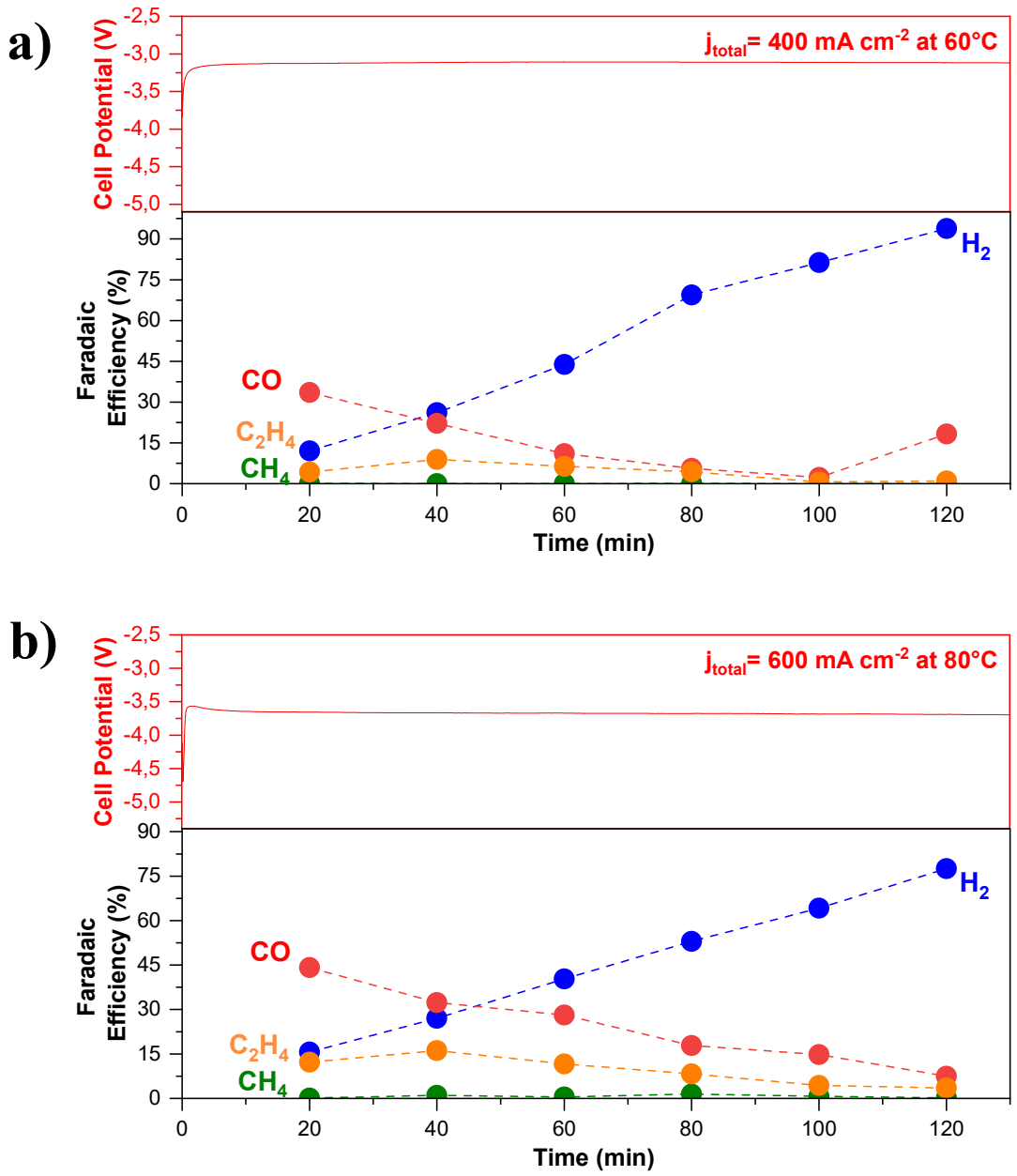

Figure S9. Product distribution and CO_2 electrolysis experiments at high current densities beyond the limiting current densities a) Performance at 400 mA cm^2 at 60°c and b) 600 mA cm^{-2} at 80°C. (Experimental conditions: Cu-GDE (Cathode), MPIP-AEM, IO_2 (Anode), CO_2 feeding rate 40 sccm, 0.1 M $KHCO_3$) .

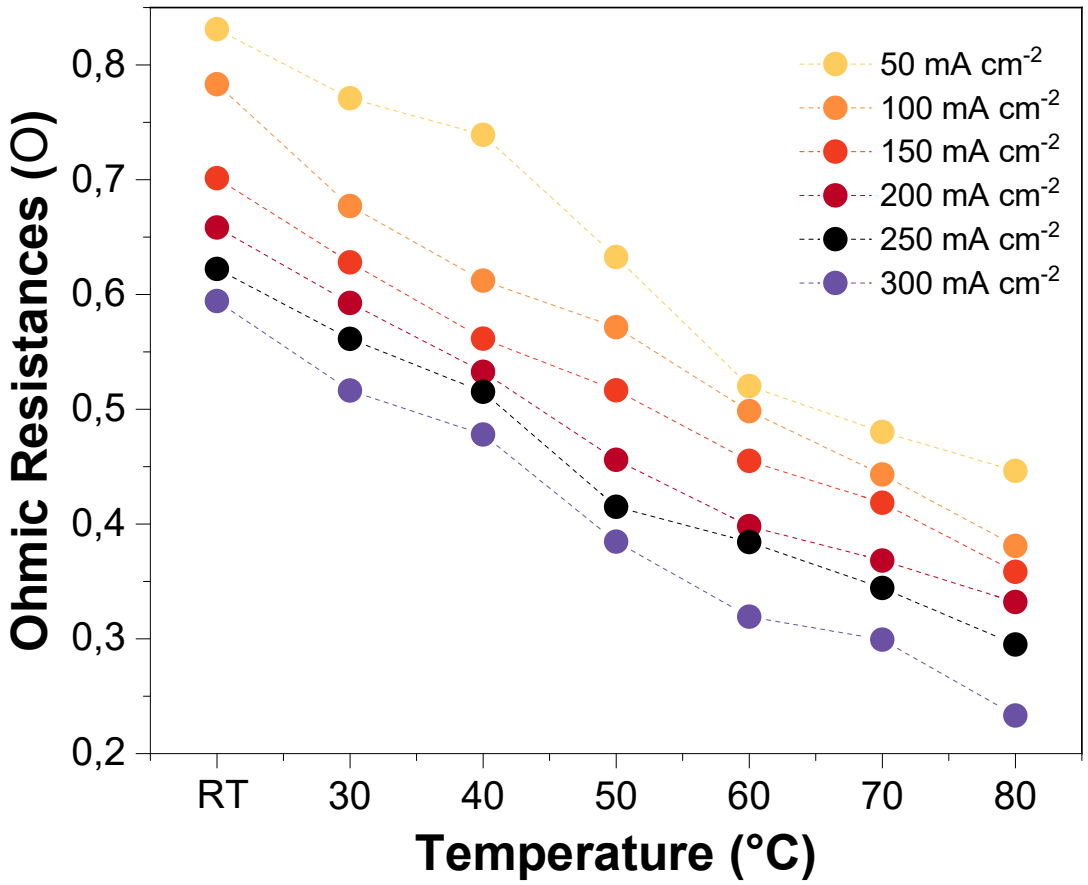

Figure S10. Measurements of ohmic resistances at different current densities and temperatures using current interrupt technique. This parameter was measured after the galvanostatic experiments. (Experimental conditions: Cu-GDE (Cathode), MPIP-AEM, IO_2 (Anode), O_2 feeding rate 40 sccm, 0.1 M $KHCO_3$) .

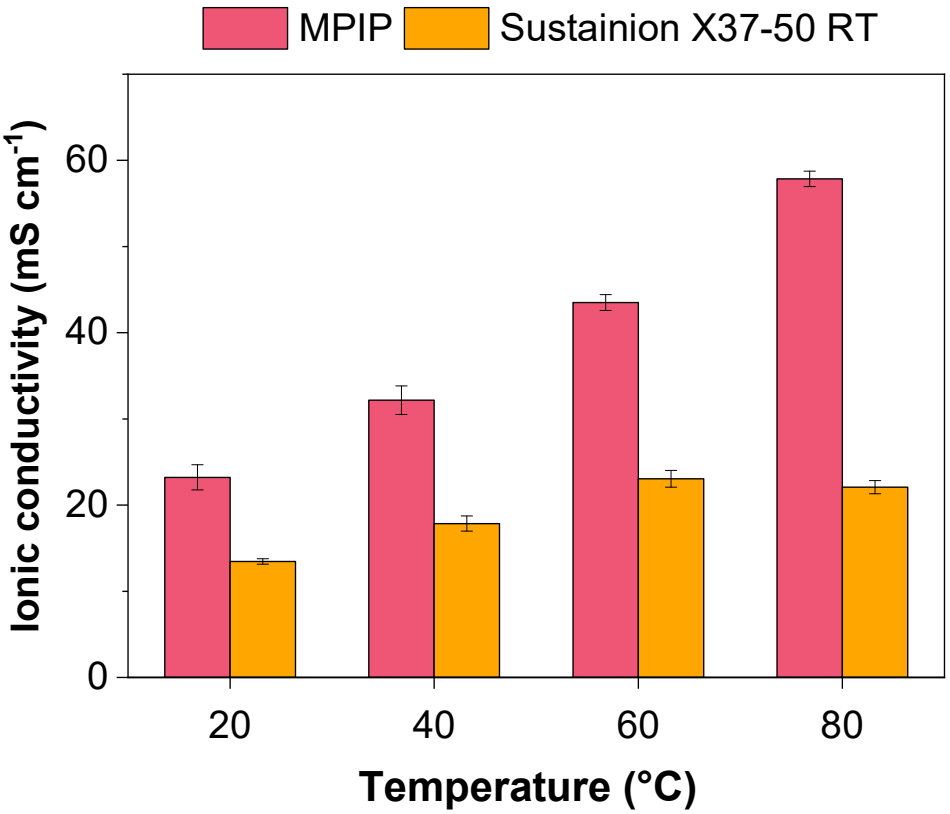

Figure S11. Measurement of the Ionic Conductivity in the HCO_3- for different AEMs (MPIP-AEM and Sustainion X37-50 RT) as a function of temperature.

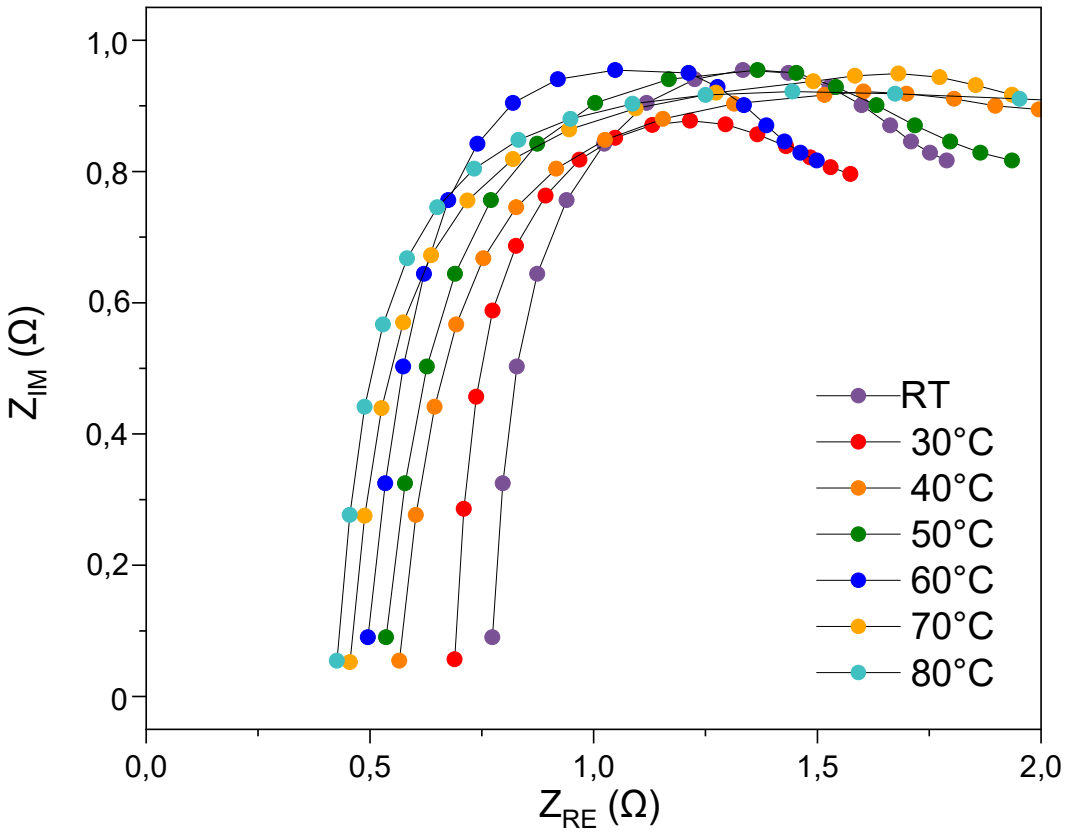

Figure S12. Galvano-electro impedance spectroscopy (GEIS) for CO_2 electrolysis at different temperatures. (High-frequency region indicates potential variations of the ionic conductivity).

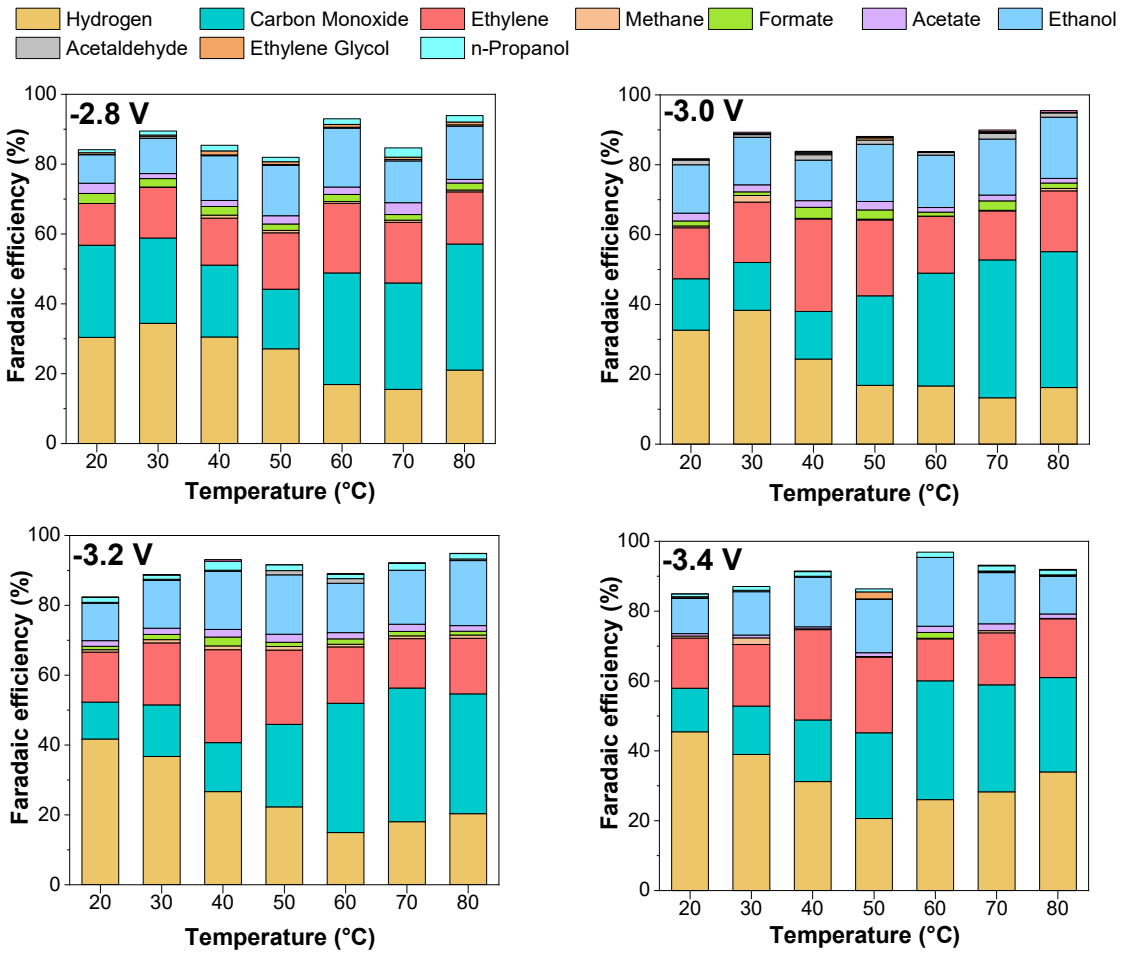

Figure S13. Product distribution as an effect of the temperature and cell potential for CO_2 electrolysis. (Experimental conditions: Cu-GDE (Cathode), MPIP-AEM, IO_2 (Anode), CO_2 feeding rate 40 sccm, 0.1 M $KHCO_3$) .

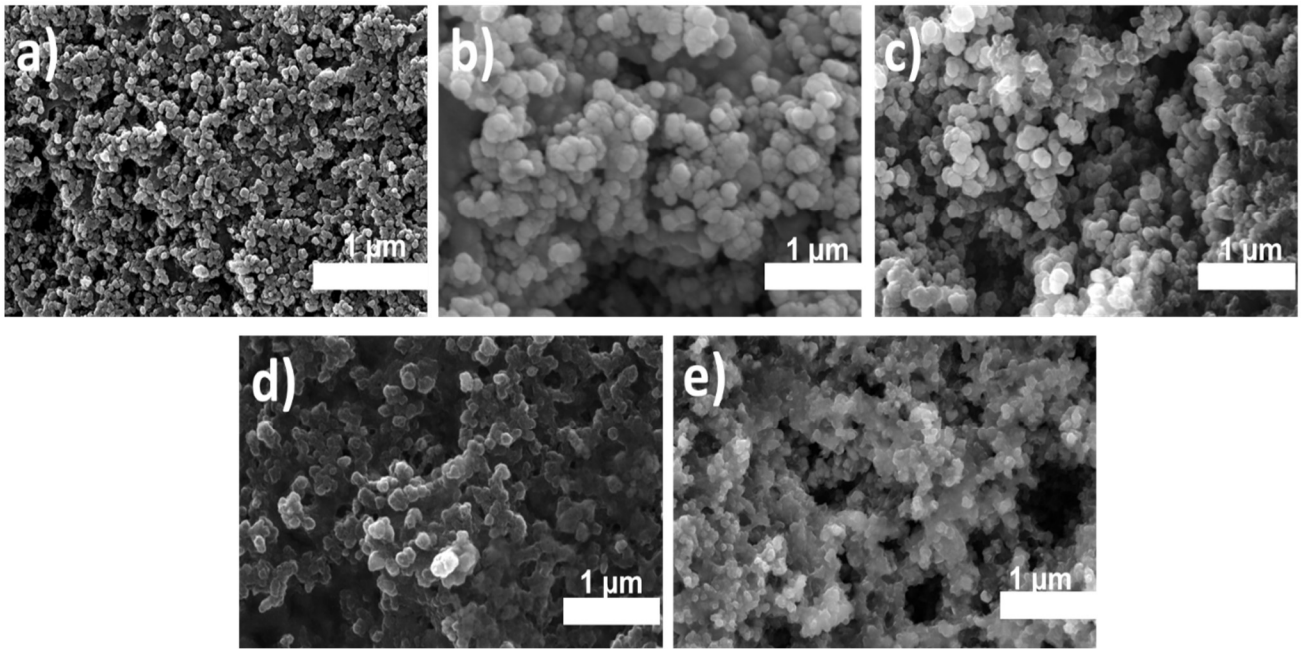

Figure S14. SEM images of the Cu-based catalyst a) gas-diffusion layer, Cu-GDEcoated on microporous carbon layers of the SG-39BB GDL at b) RT before electrolysis, c) RT after electrolysis, d) 60 °C before electrolysis and e) 60 °C after electrolysis.

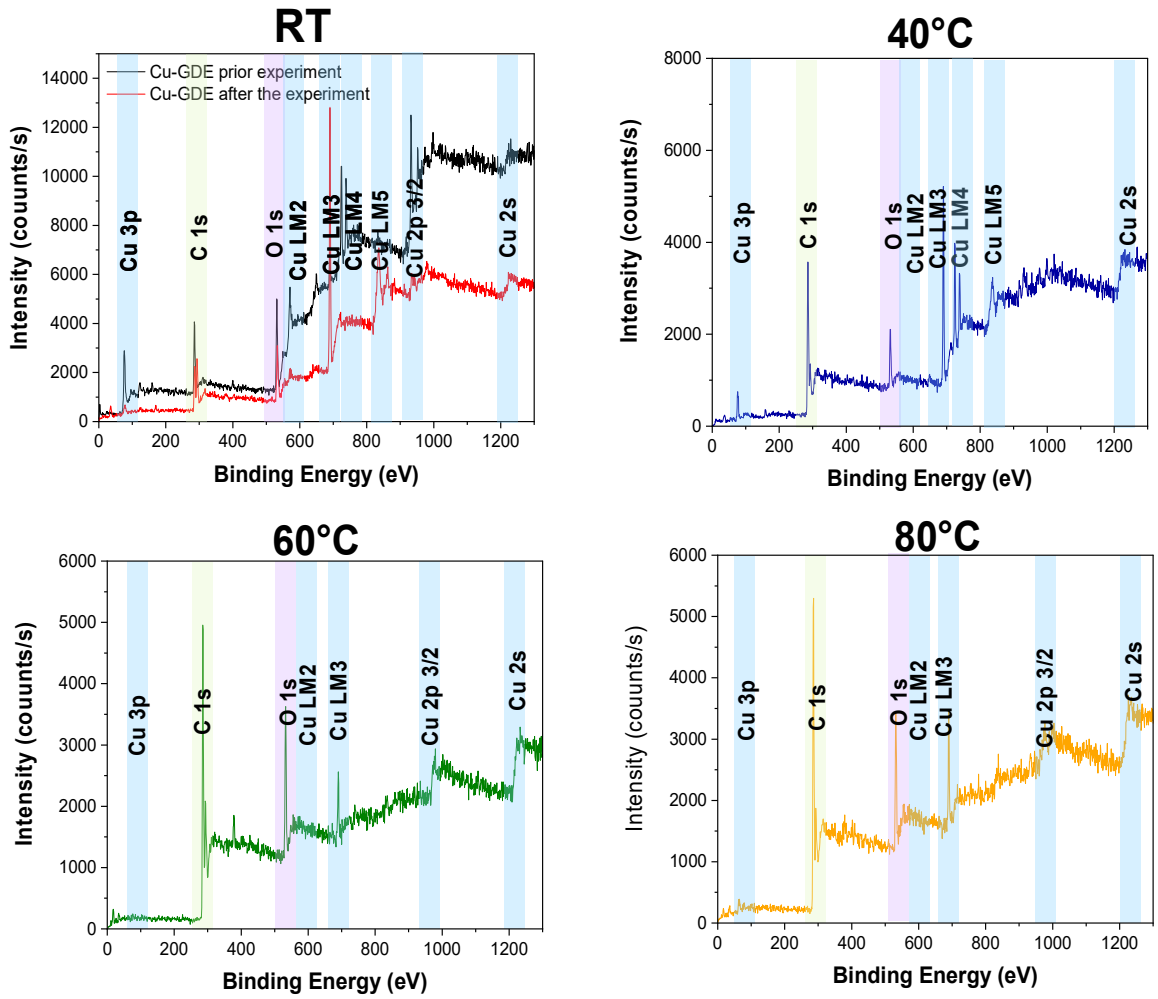

Figure S15. XPS pattern data of post-reaction Cu-GDE tested at different operating temperatures. The majority of features correspond to copper, oxygen, and carbon.

Experimental conditions for Figure S16

The cathode potential correspondence of the temperature was measured using an extra reference electrode. During assembly the 1 cm^2 electrodes were deliberately misaligned to minimize uncertainties in electrode misalignments.[22] This resulted in a final area of 0.8 cm^2. A 3.5 M Ag/AgCl reference electrode was positioned next to the cathode touching the membrane to find the cathode potential via the WE potential. The potential was subtracted by 0.2 V to convert the potential from Ag/AgCl vs SHE scales . The cathode consisted of 150 nm sputtered Cu, the anode was a commercial IrO_2 on a carbon substrate from Dioxide Materials, the AEM was MPIP, and the electrolyte was 0.1 M $KHCO_3$.

The MEA was situated in an oven, where the temperature could be accurately controlled. A thermocouple was placed inside the cell to accurately monitor the cell temperature during operation. The experiment was performed with 7 temperature steps, with room temperature, 30, 40, 50, 60, 70, and 80 ºC in one run. Each temperature was stabilized for 30 min before applying a current density. (As the room temperature was inconsistent, we did not use this point in the Figure.) The current density for every temperature step was 100 $mA \cdot cm^{-2}$.

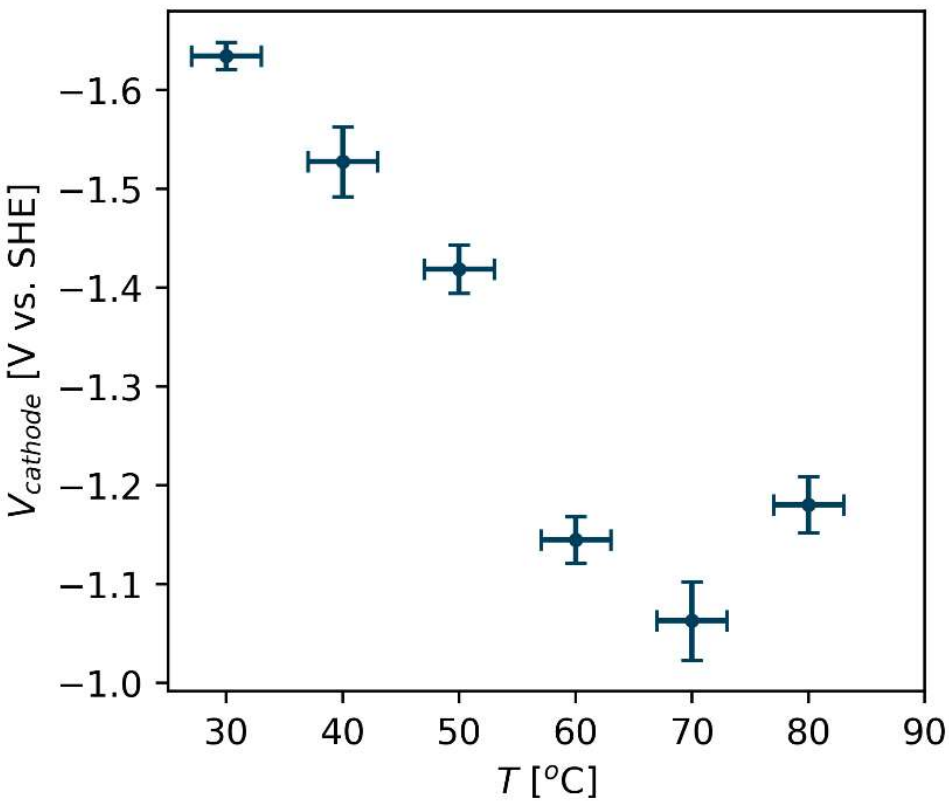

Figure S16. Cathodic potential as a function of the operating temperature. These experiments used 0.1M $KHCO_3$ and operated at 100 $mA \cdot cm^{-2}$.

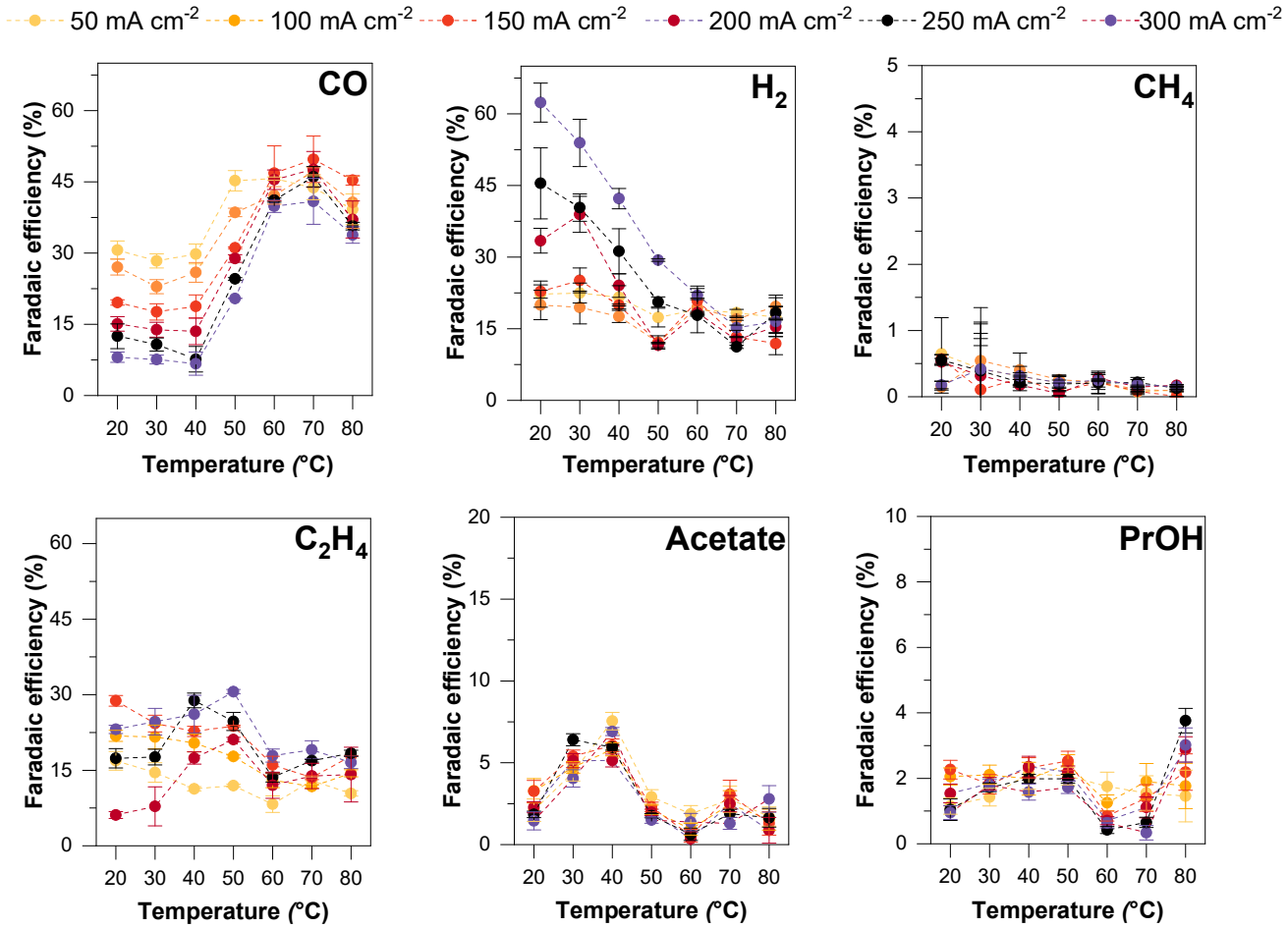

Figure S17. Trends of major electrochemical CO_2-derived products (CO, acetate, n-propanol, ethylene, methane) and HER as function of the total current density and temperature (results linked to Figure 3 of the main manuscript**).**

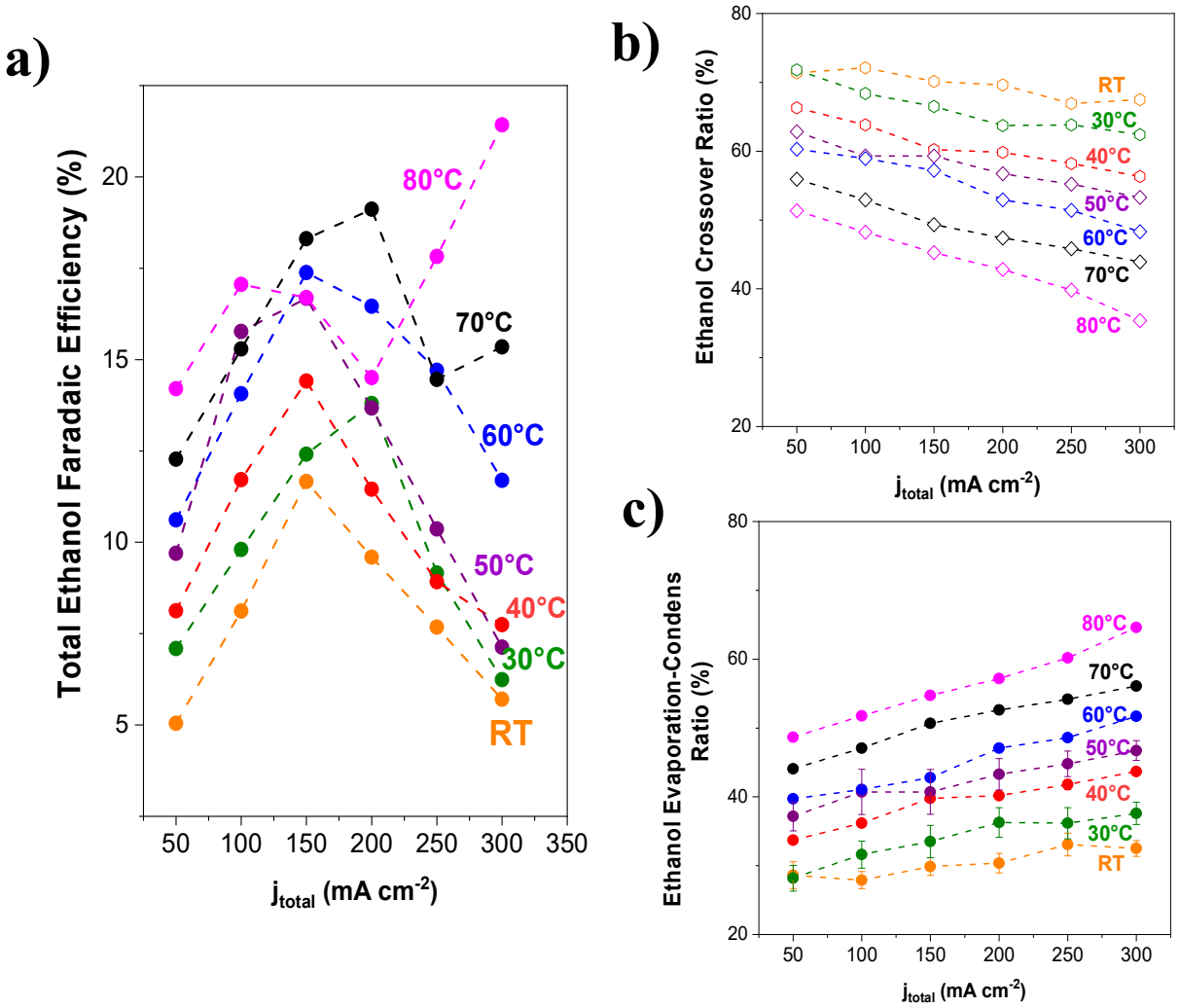

Figure S18. a). Effect of temperature in the ethanol selectivity at different total current densities b). Ethanol crossover ratio as a function of the operating temperature and the current density, and c). The evaporation rate of ethanol across the cathode-GDE is a function of the temperature. Experimental conditions: Cu-GDE (Cathode), MPIP-AEM, IO_2 (Anode), CO_2 feeding rate 40 sccm, 0.1 M $KHCO_3$. Operating time: 90 min for each measurement).

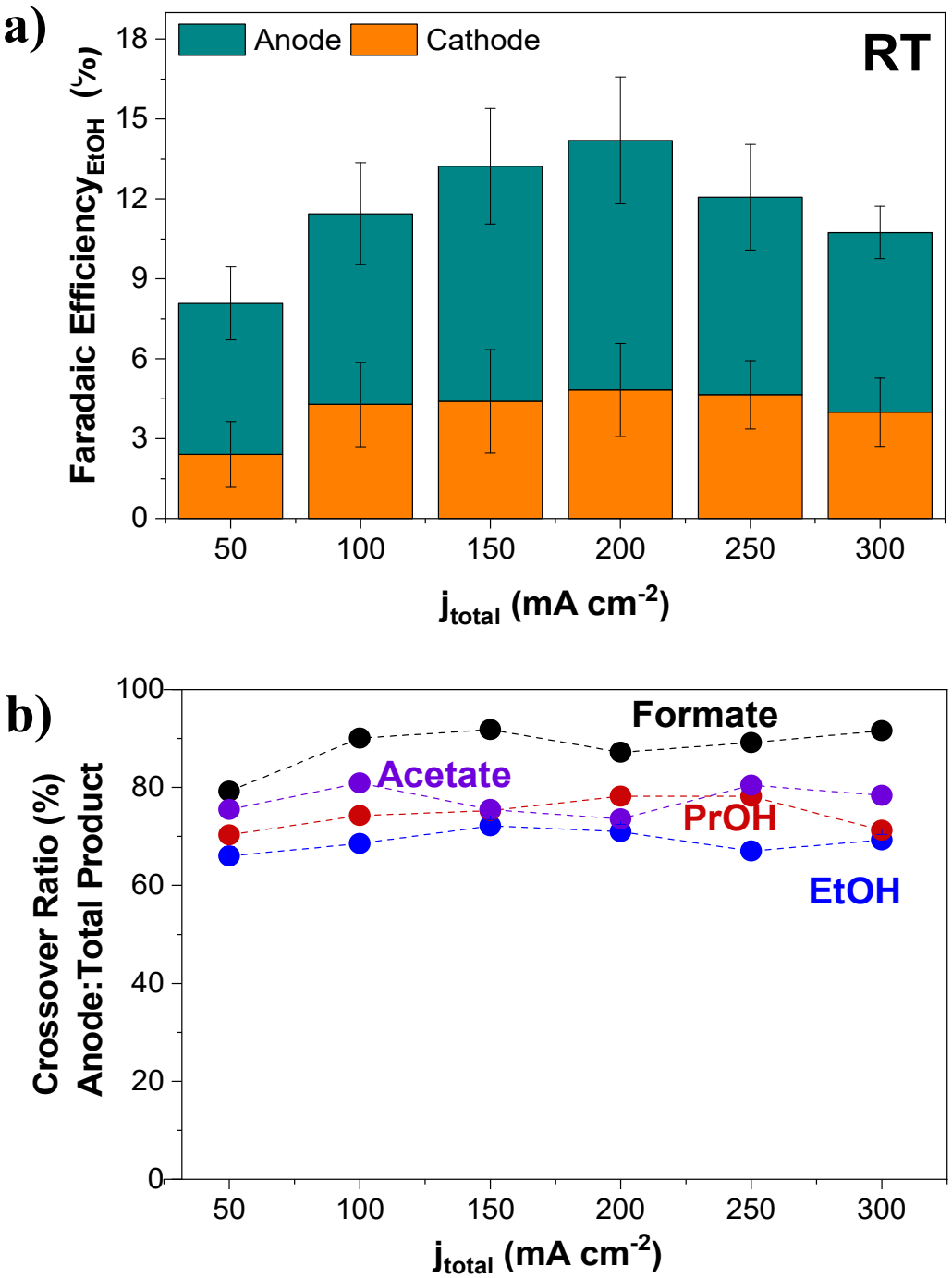

Figure S19. A crossover study of ethanol at room temperature in MEA-based CO_2 electrolysis a) Ethanol faradaic efficiencies at different current densities and quantification of the product in the cathode and anode compartments. B). Crossover ratio of product detected at the anode vs. total products for main CO_2-liquid products (ethanol, n-propanol, acetate, and formate).

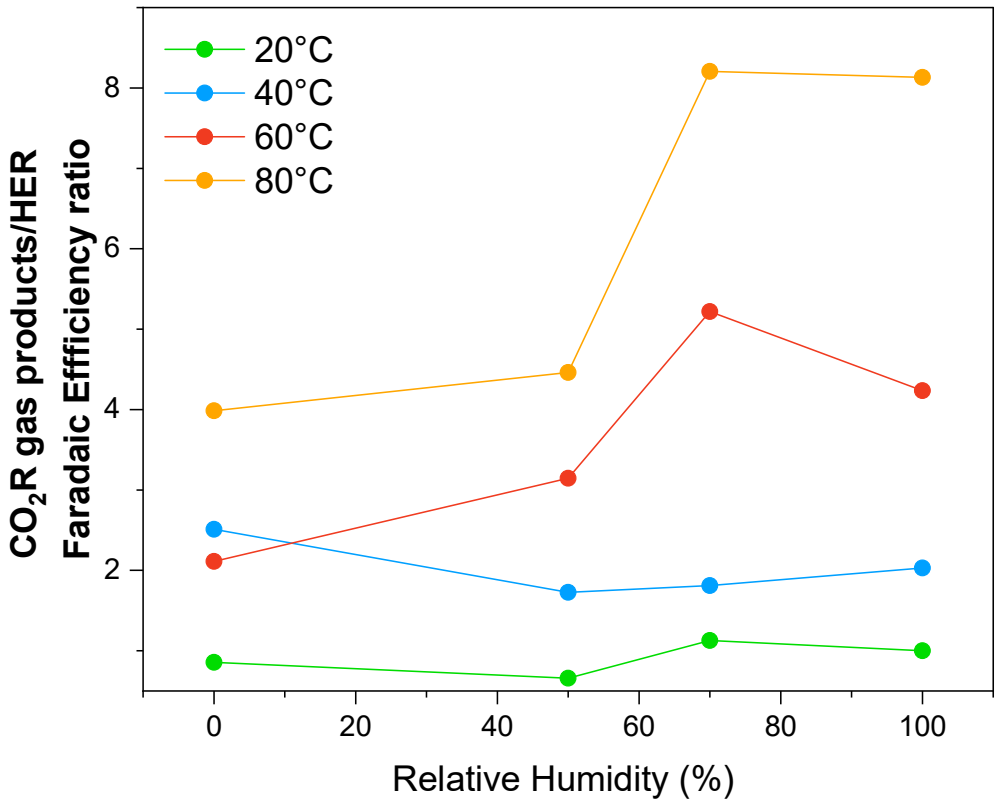

Figure S20. Effect of the relative humidity (different humidity in CO_2-inlet feed) in the product distribution of gas-products for CO_2 electrolysis as a function of the temperature. 0% means dry conditions and 100% means fully humidified. Experimental conditions: Cu-GDE (Cathode), MPIP-AEM, IO_2 (Anode), CO_2 feeding rate 40 sccm, 0.1 M $KHCO_3$. Operating time: 90 min for each measurement).

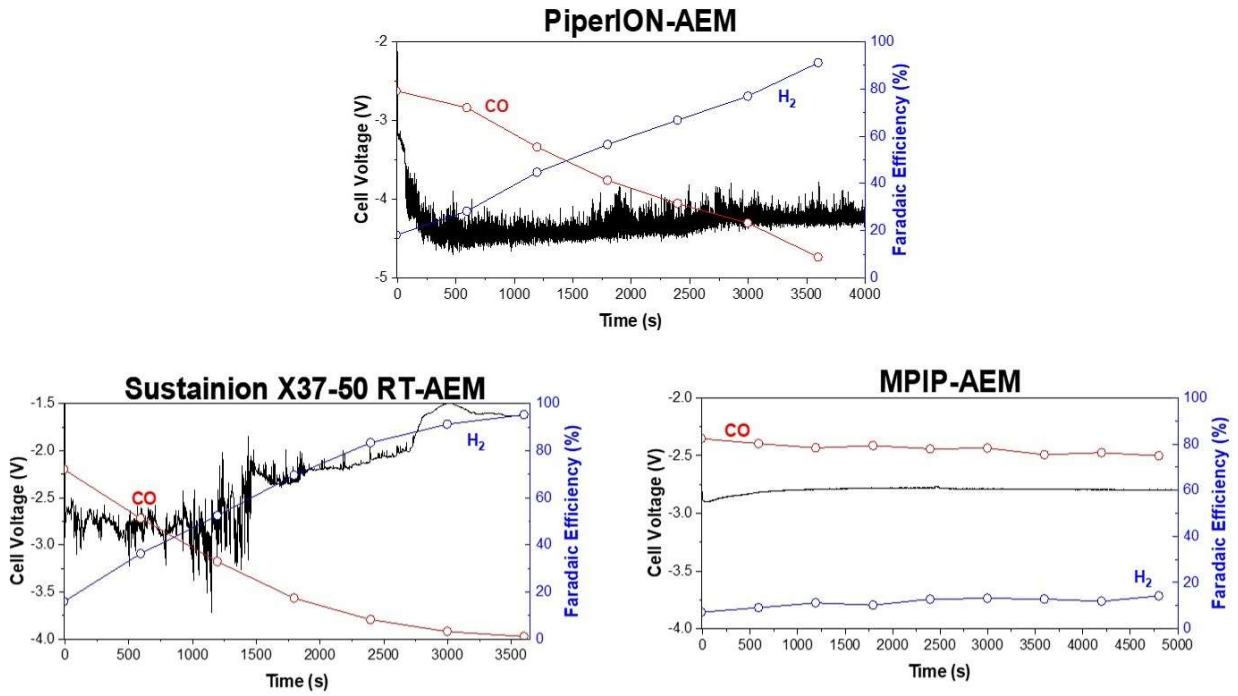

Figure S21. Effect of elevated temperature (90 °C) CO_2-electrolysis performance for different AEMs in the chemical stability over Ag-GDE. (Experimental conditions: Ag-electrocatalyst (Cathode), IrO_2 (Anode), CO_2 feeding rate 40 sccm, 0.1 M $KHCO_3$) .

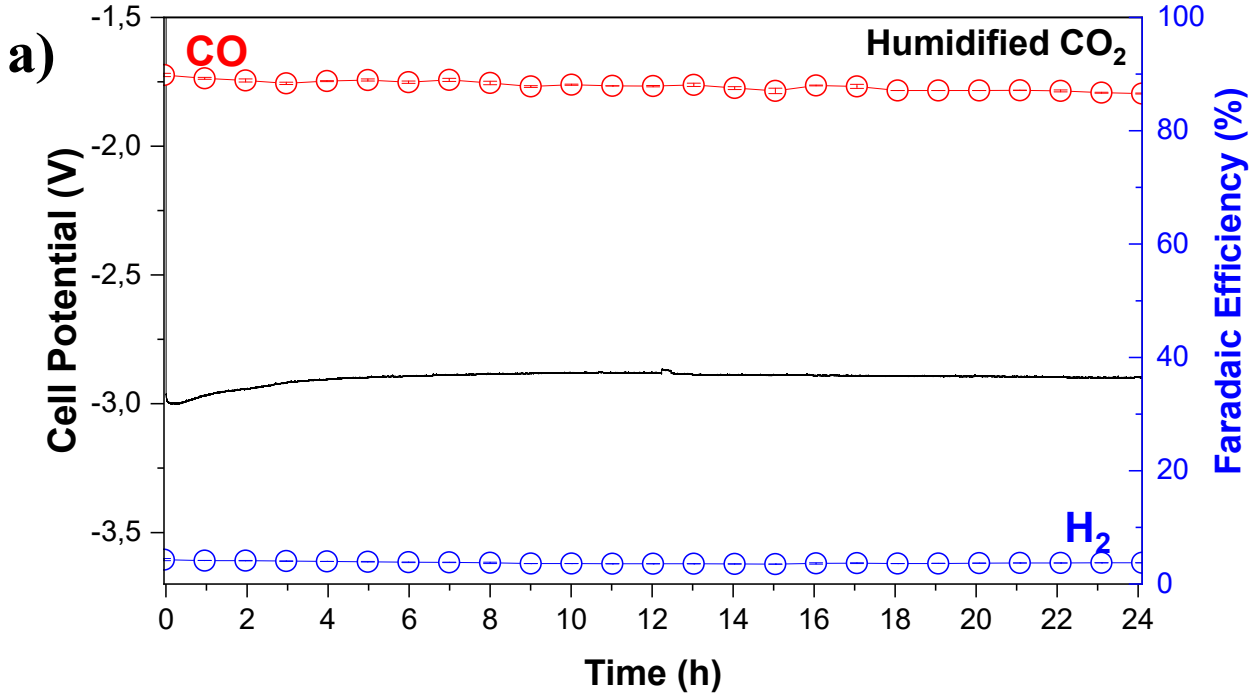

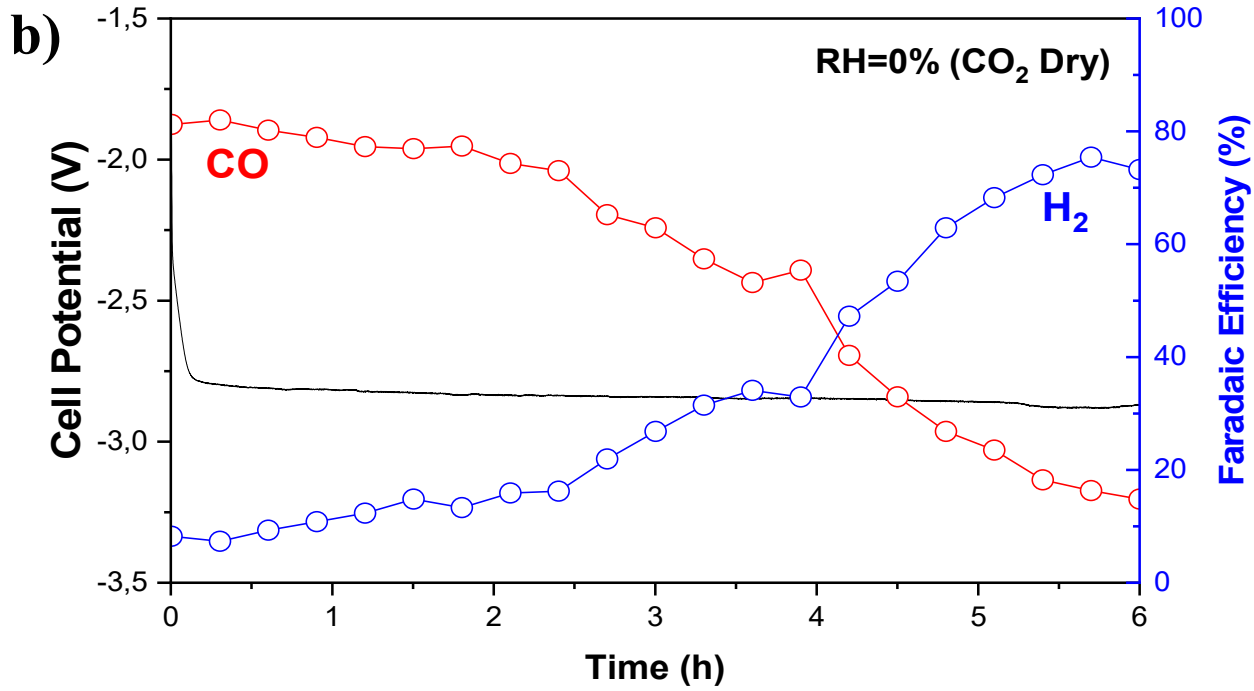

Figure S22. Coupled effect of temperature and water content by evaluating the effect of humidified CO_2 inlet vs. dry CO_2 in long-term CO_2 electrolysis at 80 °C using a Ag-GDE a). Humidified CO_2, and b). Dry CO_2

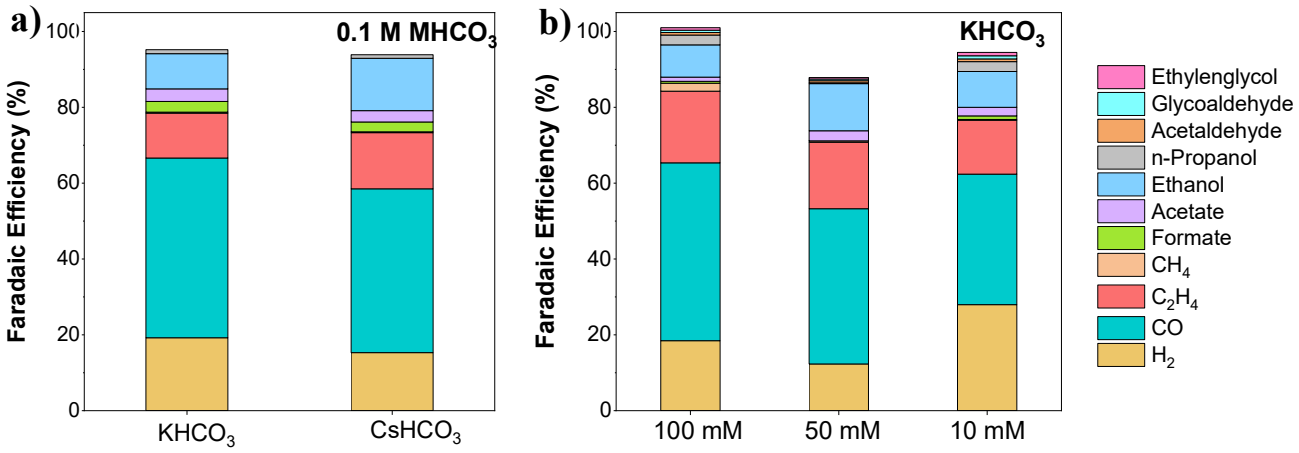

Figure S23. Study of the effect of the electrolyte at elevated temperatures (60ºC). a). Effect of the cation in the anolyte at 0.1 M. b). Effect of the electrolyte concentration for $KHCO_3$-electrolyte solutions. Experimental conditions: Cu-GDE (Cathode), MPIP-AEM, IO_2 (Anode), CO_2 feeding rate 40 sccm).

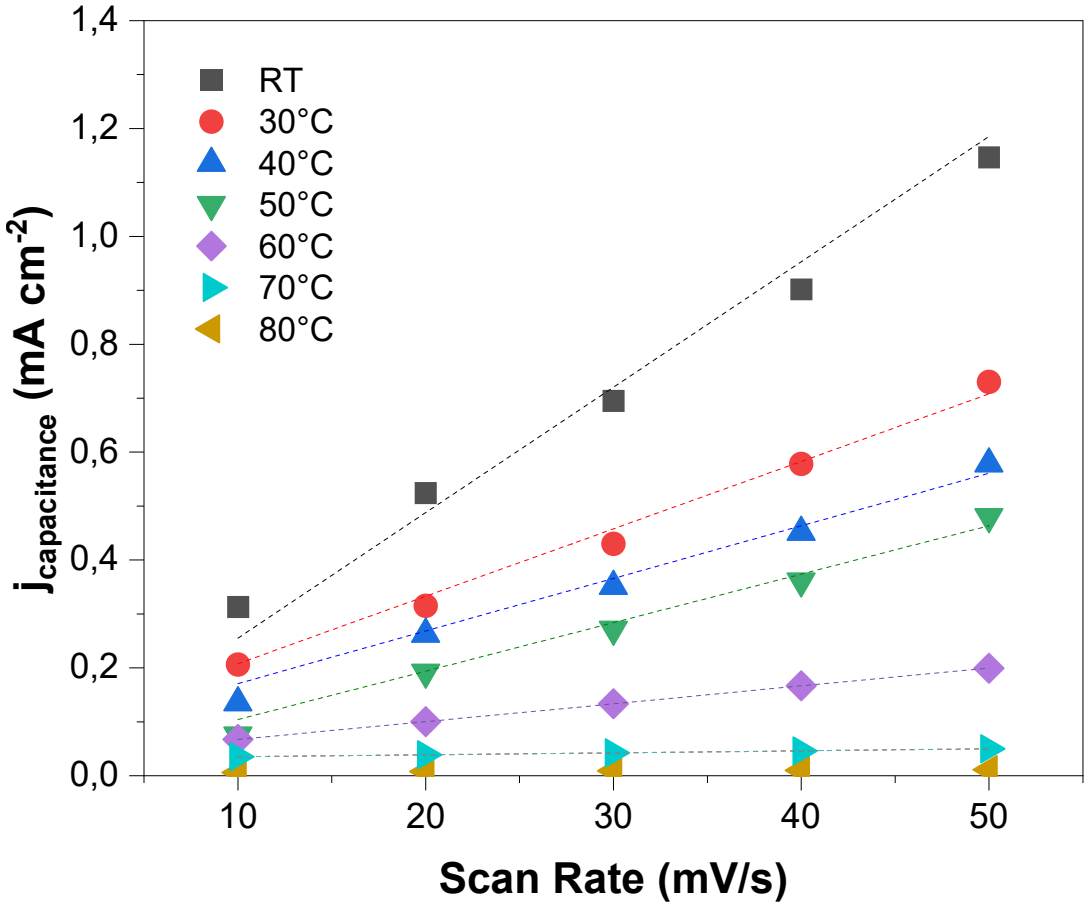

Figure S24. Electrochemical capacitance measurements after CO_2 electrolysis at different temperatures. The potential was cycled in between 0.1 and 0.35 V VS RHE at different scan rates.

Table S4. Measurements of the double-layer capacitance after CO_2 electrolysis at 200 mA cm^{-2}

Temperature (°C)	**DLC (mF cm^{-2})**
20	2.05
30	1.31
40	1.08
50	0.98
60	0.64
70	0.56
80	0.53

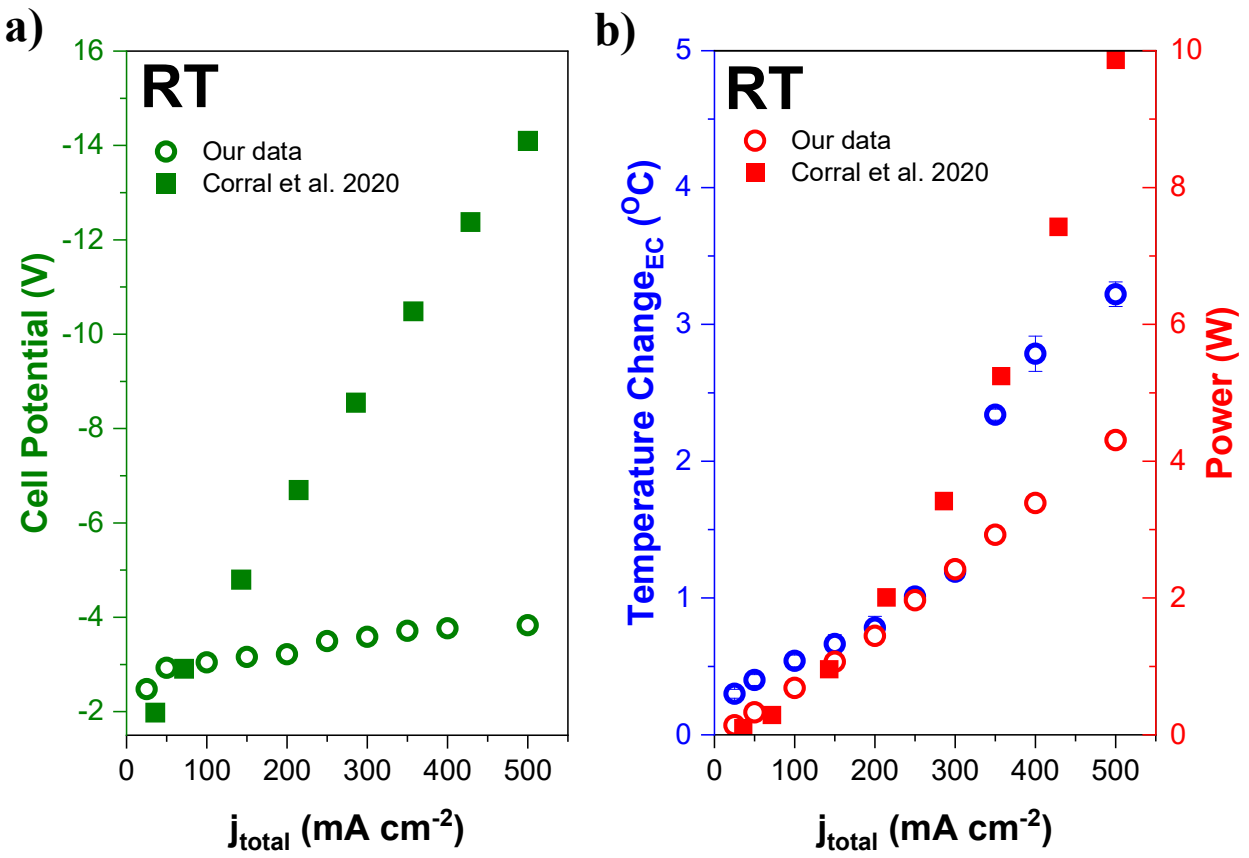

Figure S25. a). Cell potential as a function of total current density for CO_2 electrolysis b). measurements of the temperature change due to the resistive heating at room temperature at different current densities. (Experimental conditions: Cu-GDE (Cathode), MPIP-AEM, IO_2 (Anode), CO feeding rate 20 sccm, 0.1 M $KHCO_3$) . **The authors requested data from Corral et al. for a detailed data comparison between approaches.**

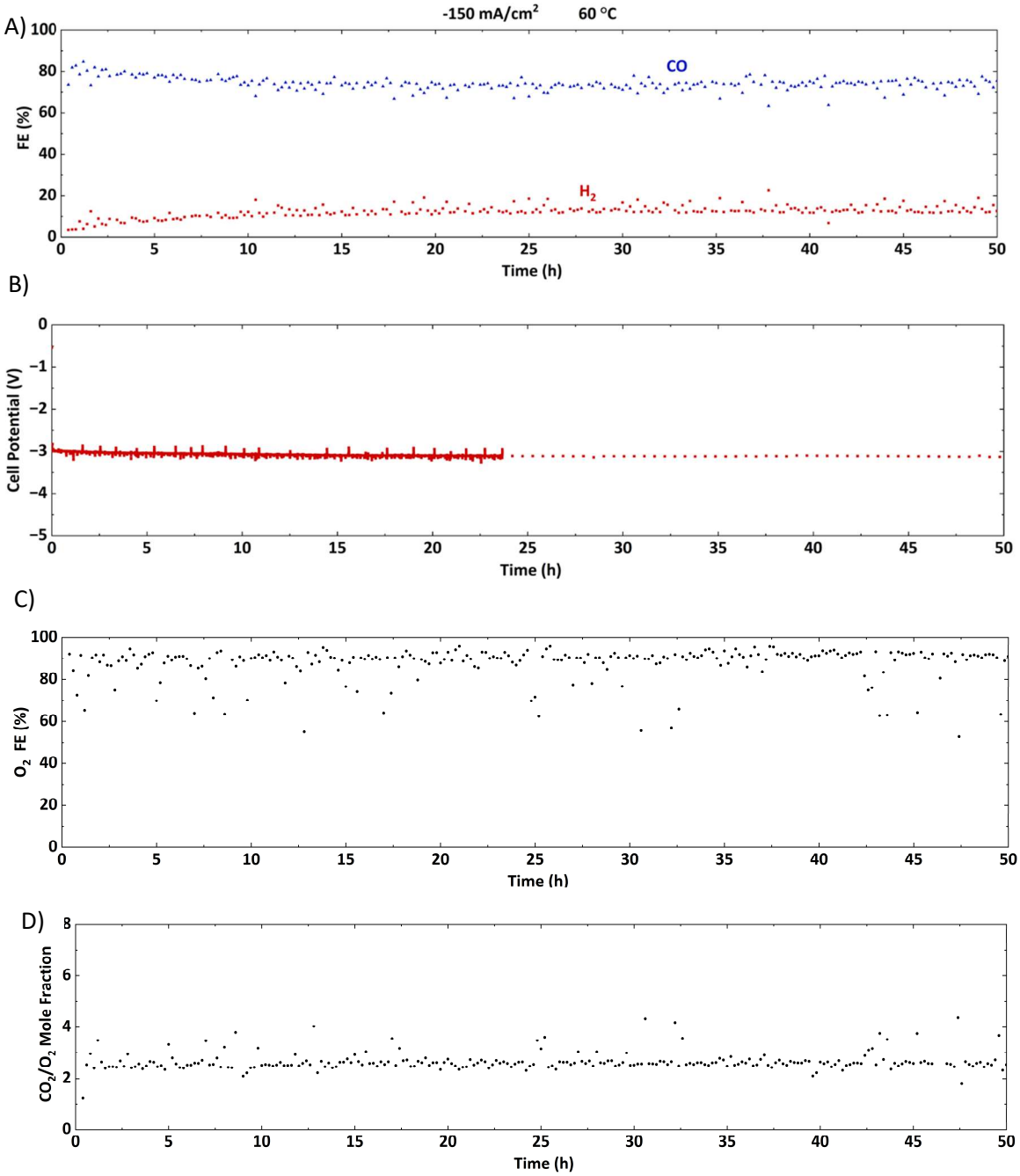

Figure S26. Effect of elevated temperature (60 °C) on CO_2-electrolysis performance with Ag-GDE. A) Cathode Faradaic efficiency, B) Potential, C) Anodic Faradaic efficiency, D) CO_2/O_2 ratio on the anode. (Experimental conditions: Ag-electrocatalyst (Cathode), IrO_2 (Anode), CO_2 feeding rate 40 sccm, 0.1 M KHCO3)

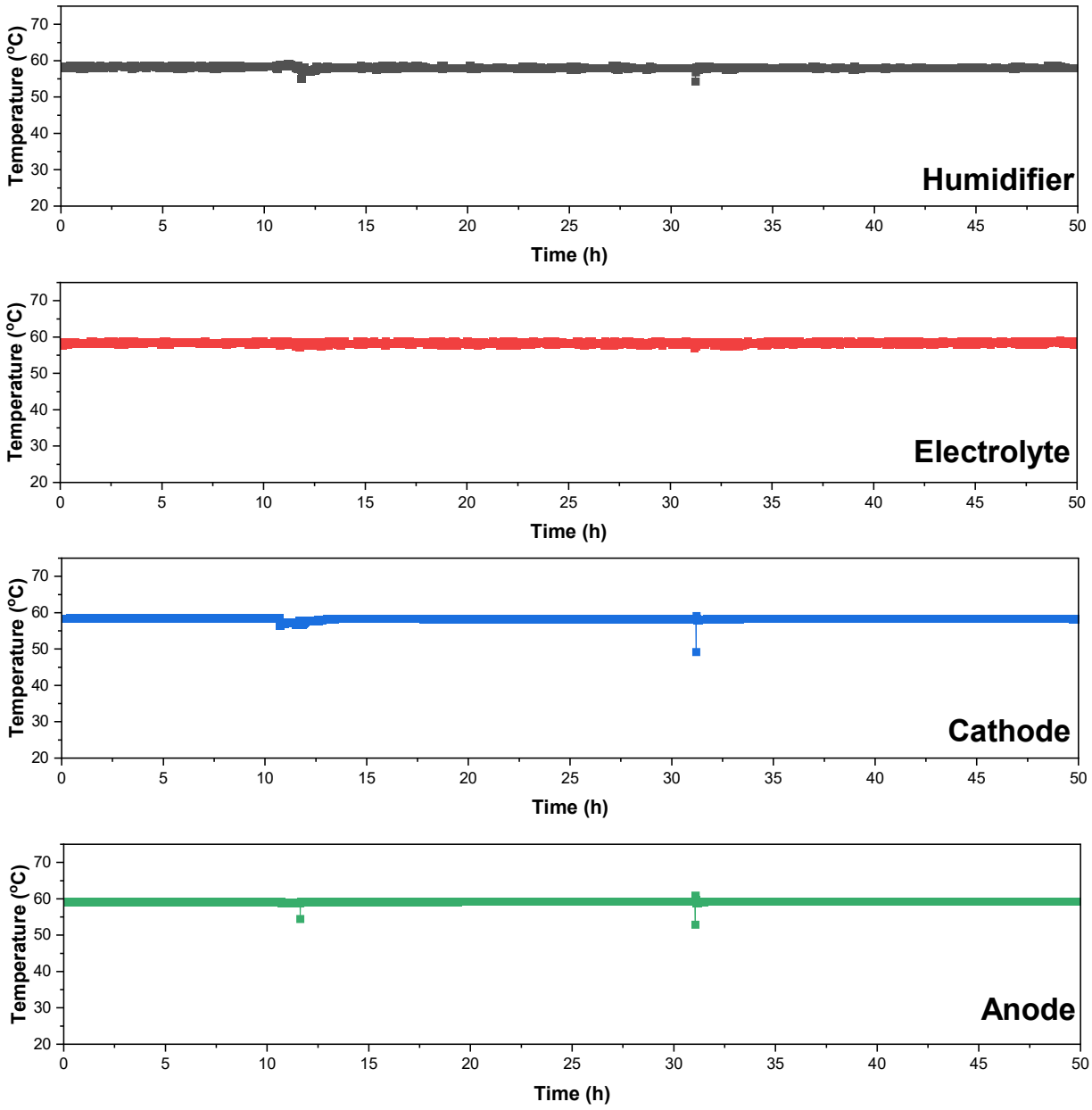

Figure S27. Temperature profile for the long-term experiment (Figure 8 of the main manuscript) for different reaction components (humidifier, electrolyte, and electrochemical cell).

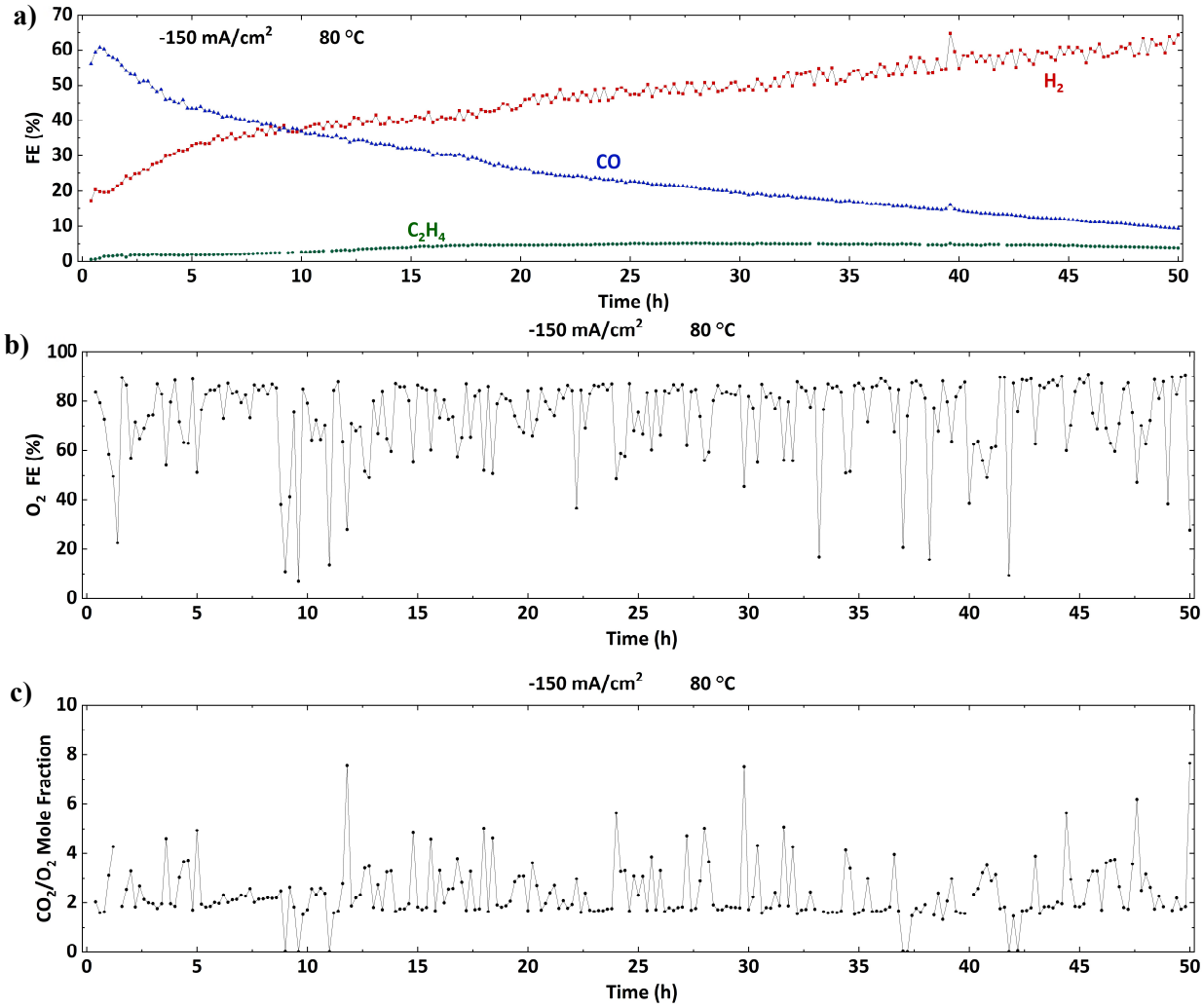

Figures S28: 50 hour CO_2 electrolysis stability test at 80 °C. A) Cathodic gas product selectivity. B) Oxygen evolution Faradaic efficiency. C) CO_2:O_2 ratio on the anode. Operating parameters were sputtered Cu cathode, MPIP membrane, IrO_2 on carbon anode. The cathode was humidified and the electrolyte was 0.1M $KHCO_3$.

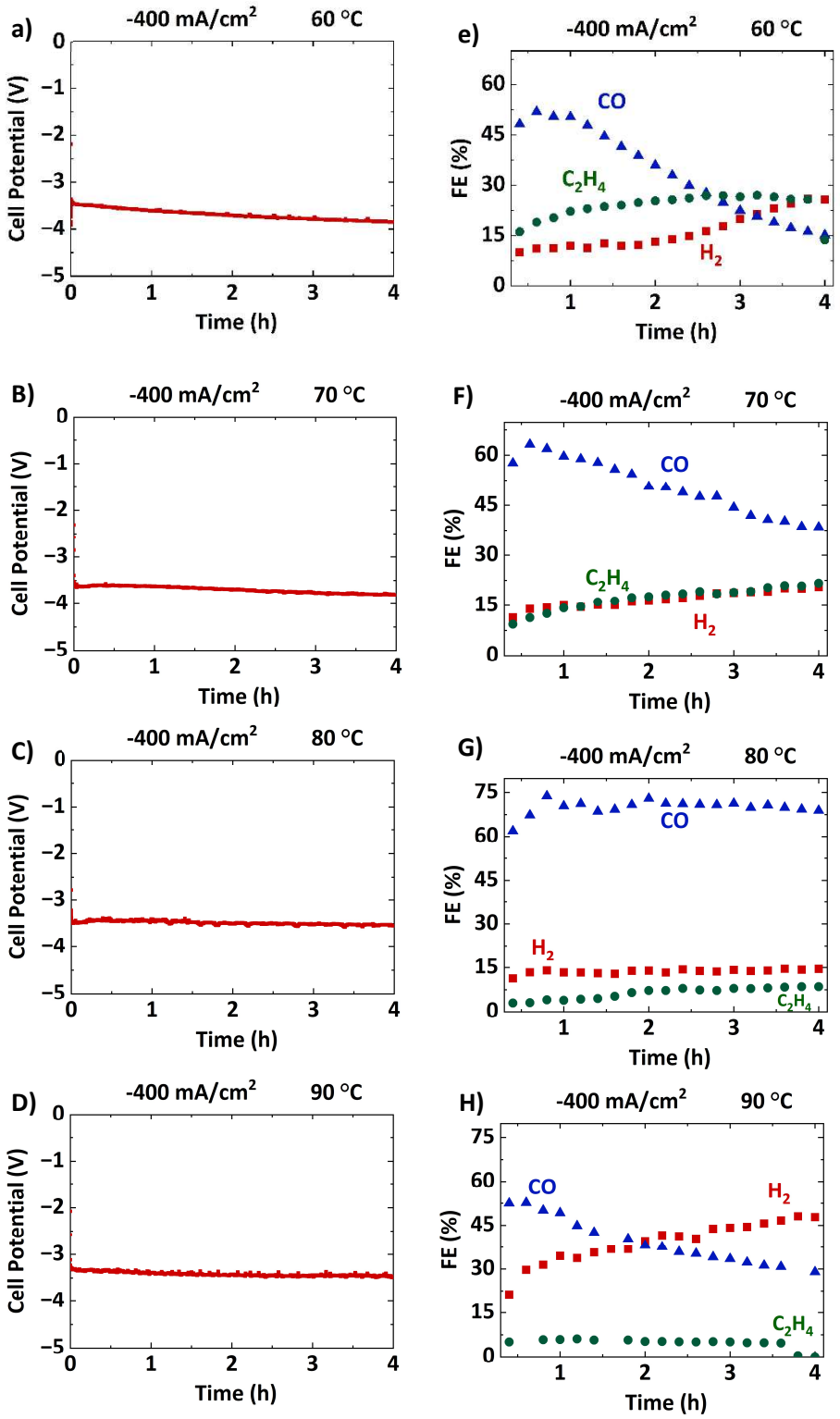

Figures S29: CO_2 electrolysis tests with Cu at 400 mA/cm^2. A-D) Cell potentials at various temperatures as a function of time. E-H) Gas product selectivity as a function of time. Operating parameters were sputtered Cu cathode, MPIP membrane, IrO_2 on carbon anode. The cathode was humidified and the electrolyte was 0.1M $KHCO_3$.

Supplementary Note III

Overall balance and influence of temperature in CO_2 electrolysis using MEA approach.[22] *We highlighted the direct parameters, mechanisms, or equations that involve temperature on it.*

Cathode Gas Channel

Overall Mass Balance: $\nabla(\rho u) = 0$

Component Mass Balance (Flux per species): $\nabla n_i = 0 \qquad i = CO_2, H_2, C_2H_4, H_2, H_2O$

Multicomponent Flux: $n_i = -\rho w_i \sum_{j=i}^{n} D_{ij}(T)\left[\frac{M_g}{M_j}\left(\nabla w_i + w_j \frac{\nabla M_g}{M_g}\right) + \left(x_j - w_j\right)\frac{\nabla p}{p}\right] + \rho u w_i$

Molas mass of gas mixture: $M_g = x_{CO2}M_{CO2} + x_{CO}M_{CO} + x_{C2H4}M_{C2H4} + x_{H2O}M_{H2O} + x_{H2}M_{H2}$

Fuller Diffusion Coefficient: $\boldsymbol{D_{ij} = \frac{0.0101325 \cdot T^{1.75}\left(\frac{1}{M_i}+\frac{1}{M_j}\right)^{0.5}}{p\left(v_i^{\frac{1}{3}}+v_j^{\frac{1}{3}}\right)}}$

Mass Fraction: $w_{CO2} + w_{CO} + w_{C2H4} + w_{H2} + w_{H2O} = 1$

Gas and liquid-water transport in the GDL and CL (Porous Media)

Overall Mass Balance: $\nabla(\rho u) = Q$

Mass Source Term (Q): $Q = R_{CO2} + R_{CO} + R_{H2} + R_{H2O}$

The mass-average velocity field of phase (Darcy's Law): $u_p = -\frac{k}{\mu}\nabla p$

Permeability (On the GDL using Tomadakis-Sotirchos model): $k = \frac{\varepsilon}{8\,(\ln\ )^2}\frac{(\varepsilon-\varepsilon_p)^{\alpha+2} r_f^2}{\varepsilon(1-\varepsilon_p)^{\alpha}[(\alpha+1)(\varepsilon-\varepsilon_p)]^2}$

Component Mass Balance: $\nabla n_i = R_i = R_{CT,i} + R_{B,i} + R_{PT,i} \qquad i = CO_2, H_2, C_2H_4, H_2, H_2O$

Molar Flux (from the mass flux): $n_i = -\rho w_i \sum_{j=1}^{N} D_{ij}^{eff}\left[\frac{M_g}{M_j}\left(\nabla w_j + w_j \frac{\nabla M_g}{M_g}\right) + \left(x_i - w_j\right)\frac{\nabla p}{p}\right] + \rho u w_i$

Effective gas diffusivity (Bruggeman correction): $D_{ij}^{eff} = \varepsilon^{1.5} D_{ij}$

Mole Fraction: $\sum x_i = 1 \qquad x_i = \frac{w_i M_g}{M_i}$

<u>Charge transfer reaction in CL (R_{CT})</u>

Charge conservation: $\nabla i = 0$

Current Density (Ohm's law): $i = -\sigma_{GDL}\nabla\phi_s$

Overpotential: $\eta_k = (\phi_S - \phi_L) - \left(U_k^0 - \frac{2.303RT}{F}\right) pH$

Reaction Rate Charge transfer: $R_{CT.I} = -M_i \sum_k \frac{s_i k a_v i_k}{zF}$

Charge transfer reactions per species: $\boldsymbol{i_k = -i_{0,k}\left(\frac{c_j}{c_j^{ref}}\right)^{\gamma_k} \exp\left(\frac{-\alpha_{c,k}F}{RT}\eta_k\right)}$

Exchange current density: $\boldsymbol{i_{0,k} = A_K \exp\left(-\frac{E_{a,k}}{RT}\right)}$

Current Source Terms associated with solid phase: $S_s = \left(-\sigma_{CL,s}\nabla\phi_s\right) = -a_i i_i$

Current Source Terms associated with the liquid phase: $S_l = \left(-\sigma_{CL,l}\nabla\phi_l\right) = a_i i_i$

<u>Electrolyte</u>

Current Density (Ohm's law): $i = -\sigma_{electrolyte}\nabla\phi_l$

Ionomer/membrane

Water flux: $n_w = -\alpha_w^{eff}\nabla\mu_w + \sum_j \epsilon_j^{eff} n_j$

Electro-osmotic coefficient: $\sum_j \epsilon_j^{eff} n_j = \epsilon_j^{eff}\frac{i_L}{F}$

Water activity: $a_w = \frac{p_v}{p_w^{vap}}$

Water mole fraction in the Ionomer: $x_w = \frac{\lambda}{1+\lambda}$

Water volume fraction in the Ionomer: $\beta_L = \frac{\lambda V_W}{\lambda V_W + \left(\frac{1}{IEC\,\rho_M}\right)}$

Chemical Potential Water: $\boldsymbol{\mu_w = RT\ln(a_w) + \beta_L * (p_{L,M} - p^{ref})}$
Concentration CO_2 at the CL/ionomer interface: $\boldsymbol{c^G_{CO2} = H_{CO2}(T)p_G y_{CO2}}$
Equilibrium water Liquid/vapor CL/ionomer interface: $c^G_w = c_M\lambda \qquad w_w = \frac{p_{sat}M_w}{pM_g}$
Donnan Potential (potential difference membrane/electrolyte) interface: $\Delta\phi_D = \phi^M_l - \phi^E_l$
Equilibrium species between Ionomer and electrolyte: $c^M_i = c^E_i\left(-\frac{z_iF}{RT}\Delta\phi_D\right)$
Molar Flux other liquid species: $n_{j\neq w} = -D^{eff}_j\nabla c_j - \frac{z_jF}{RT}\ D^{eff}_j c_j\nabla\phi_L$
Electroneutrality: $\sum_j z_j c_j = 0$

Bulk reactions (homogeneous reactions $R_{B,i}$)
Reaction rate due to homogeneous reactions: $R_{B,i} = M_i\sum s_{i,n}\ \left(k_n\prod_{s_{i,n}} c_i^{-s_{i,n}} - \frac{k_n}{K_n}\prod_{s_{i,n}} c_i^{s_{i,n}}\ \right)$
Equilibrium constants (Van't Hoff equations): $\boldsymbol{K_n = \exp\left(\frac{\Delta S_n}{R}\right)\exp\left(-\frac{\Delta H_n}{RT}\right)}$

Phase transfer (rate of mass transfer between phases of CO_2, water, and liquid products) $R_{PT,i}$
Phase transfer of CO_2 and liquid products: $R_{PT,i,I}\ (CL) = a_s k_{MT,i}\left(c^{eq}_i - c_i\right)$
Phase transfer of water into the Ionomer: $\boldsymbol{R_{PT,w,ionomer} = a_s K_{MT}\left(\frac{RH}{100} - a_w\right) + \frac{a_s k_{MT,L}}{RT}\left(p_L - p_{L,M}\right)}$
Relative humidity of the Gas-phase: $R_H = \frac{p_G y_0}{p_o^{sat}}$
Phase transfer of water in the gas phase: $R_{PT,w,G} = -a_s K_{MT}\left(\frac{RH}{100} - a_w\right) - K_{MT}(RH - 100\%)\ \left[H_0\left(\frac{p_L}{p^{ref}} + H_0(RH - 100\%)\right]\right.$
Phase transfer of water in the gas phase: $\boldsymbol{R_{PT,w,L} = -\frac{a_s K_{MT}}{RT}(p_L - p_{L,M}) + K_{MT}(RH - 100\%)\ \left[H_0\left(\frac{p_L}{p^{ref}} + H_0(RH - 100\%)\right]\right.}$

Overall Mass Balance associated with phase transfer
Gas phase: $Q_G = -M_{CO2}R_{PR,CO}\ + M_W R_{PT,W,G} + \sum M_i R_{CT,i}$
Liquid phase: $Q_L = M_W R_{PT,W,L}$

Anode CL

Overpotential: $\eta_k = (\phi_S - \phi_L) - \left(U^0_k - \frac{2.303RT}{F}\right)\ pH$
Mass balance in the anode: $Q = R_{CT} = R_{O2} + R_{H2O}$
Charge transfer reactions per species: $\boldsymbol{i_k = -i_{0,k}\left(\frac{c_j}{c_j^{ref}}\right)^{\gamma_k}\exp\left(\frac{-\alpha_{c,k}F}{RT}\eta_k\right)}$
Exchange current density: $\boldsymbol{i_{0,k} = A_K\exp\left(-\frac{E_{a,k}}{RT}\right)}$
Overall Cell Potential: $E_{cell} = E_{cat} - E_{an}$
Reaction Rate OER: $R_{O2} = \frac{a_{O2}i_{O2}}{4F}\ M_{O2}$
Reaction Rate water: $R_{H2O} = \frac{a_{O2}i_{O2}}{2F}M_{H2O}$

Heat balance

Overall heat balance: $Q_H = Q_{CT} + Q_B + Q_J$
Heat generated from charge transfer reactions: $Q_{CT} = \sum_K(i_k\,\eta_k + i_k\,\cup_k)$
Peltier coefficient for HER: $\boldsymbol{\cup_K = 240\ \frac{T[K]}{298}}$
Peltier coefficient for OER: $\boldsymbol{\cup_K = 13\ \frac{T[K]}{298}}$
Peltier coefficient for COER: $\boldsymbol{\cup_K = 240\ \frac{T[K]}{298}}$
Heat generated from homogeneous bulk bicarbonate: $Q_B = \sum_n \Delta H_n\ \left(k_n\prod_{s_{i,n}} c_i^{-s_{i,n}} - \frac{k_n}{K_n}\prod_{s_{i,n}} c_i^{s_{i,n}}\ \right)$
Joule heating (due to electrical resistance): $Q_j = i_s^2/\sigma_m$

References

1 F. Pelayo García de Arquer, C.-T. Dinh, A. Ozden, J. Wicks, C. McCallum, A. R. Kirmani, D.-H. Nam, C. Gabardo, A. Seifitokaldani, X. Wang, Y. C. Li, F. Li, J. Edwards, L. J. Richter, S. J. Thorpe, D. Sinton and E. H. Sargent, *Science, 2020, **267**, 661-666*

2 L. C. Weng, A. T. Bell and A. Z. Weber, *Energy Environ Sci*, 2019, **12**, 1950–1968.

3 A. Fenghour, W. A. Wakeham and V. Vesovic, *J Phys Chem Ref Data*, 1998, **27**, 31–39.

4 R. Fernández-Prini, J. L. Alvarez and A. H. Harvey, *J Phys Chem Ref Data*, 2003, 32, 903–916.

5 B. Endrdi, E. Kecsenovity, A. Samu, T. Halmágyi, S. Rojas-Carbonell, L. Wang, Y. Yan and C. Janáky, *Energy Environ Sci*, 2020, **13**, 4098–4105.

6 E. J. Dufek, T. E. Lister and M. E. McIlwain, *J Appl Electrochem*, 2011, **41**, 623–631.

7 Z. Yin, H. Peng, X. Wei, H. Zhou, J. Gong, M. Huai, L. Xiao, G. Wang, J. Lu and L. Zhuang, *Energy Environ Sci*, 2019, **12**, 2455–2462.

8 B. Pribyl-Kranewitter, A. Beard, T. Schuler, N. Diklić and T. J. Schmidt, *J Electrochem Soc*, 2021, **168**, 043506.

9 C. M. Gabardo, C. P. O'Brien, J. P. Edwards, C. McCallum, Y. Xu, C. T. Dinh, J. Li, E. H. Sargent and D. Sinton, *Joule*, 2019, **3**, 2777–2791.

10 R. K. Miao, Y. Xu, A. Ozden, A. Robb, C. P. O'Brien, C. M. Gabardo, G. Lee, J. P. Edwards, J. E. Huang, M. Fan, X. Wang, S. Liu, Y. Yan, E. H. Sargent and D. Sinton, *Joule*, 2021, **5**, 2742–2753.

11 W. Lee, Y. E. Kim, M. H. Youn, S. K. Jeong and K. T. Park, *Angewandte Chemie*, 2018, **130**, 6999–7003.

12 H. Li and C. Oloman, *J Appl Electrochem*, 2007, **37**, 1107–1117.

13 E. J. Dufek, T. E. Lister and S. G. Stone, *J Appl Electrochem*, 2014, **44**, 849–855.

14 E. Jeng and F. Jiao, *React Chem Eng*, 2020, **5**, 1768–1775.

15 A. Löwe, C. Rieg, T. Hierlemann, N. Salas, D. Kopljar, N. Wagner and E. Klemm, *ChemElectroChem*, 2019, **6**, 4497–4506.

16 S. Nitopi, E. Bertheussen, S. B. Scott, X. Liu, A. K. Engstfeld, S. Horch, B. Seger, I. E. L. Stephens, K. Chan, C. Hahn, J. K. Nørskov, T. F. Jaramillo and I. Chorkendorff, *Chem Rev*, 2019, 119, 7610–7672.

17 M. E. Leonard, L. E. Clarke, A. Forner-Cuenca, S. M. Brown and F. R. Brushett, *ChemSusChem*, 2020, **13**, 400–411.

18 J. Giner and C. Hunter, *The Mechanism of Operation of the Teflon-Bonded Gas Diffusion Electrode: A Mathematical Mode*, J.Electrochem.Soc, 1969, **116**, 1124

19 L. C. Weng, A. T. Bell and A. Z. Weber, *Physical Chemistry Chemical Physics*, 2018, **20**, 16973–16984.

20 P. Linstrom and G. Mallard, .BSRL Book, 2001

21 L. C. Weng, A. T. Bell and A. Z. Weber, *Energy Environ Sci*, 2020, **13**, 3592–3606.

22 R. Zeng, R.C.T Slade and J.R. Varcoe, *Electrochimica Acta*, 2010, Vol.56(1), pp.607-619